

## RESEARCH ARTICLE

10.1002/2014JD022180

## Special Section:

Fast Physics in Climate Models: Parameterization, Evaluation and Observation

## Key Points:

- Upstream convection controls isotopic composition
- Isotopic composition is more influenced by encountered convection
- Condensation over foothill is the most important process

## Correspondence to:

J. Gao,  
JingGao@itpcas.ac.cn

## Citation:

He, Y., et al. (2015), Impact of atmospheric convection on south Tibet summer precipitation isotopologue composition using a combination of in situ measurements, satellite data and atmospheric general circulation modeling, *J. Geophys. Res. Atmos.*, 120, 3852–3871, doi:10.1002/2014JD022180.

Received 23 JUN 2014

Accepted 1 APR 2015

Accepted article online 7 APR 2015

Published online 11 MAY 2015

# Impact of atmospheric convection on south Tibet summer precipitation isotopologue composition using a combination of in situ measurements, satellite data, and atmospheric general circulation modeling

You He<sup>1,2,3</sup>, Camille Risi<sup>3</sup>, Jing Gao<sup>2,4</sup>, Valérie Masson-Delmotte<sup>5</sup>, Tandong Yao<sup>2,4</sup>, Chun-Ta Lai<sup>6</sup>, Yongjian Ding<sup>1</sup>, John Worden<sup>7</sup>, Christian Frankenberg<sup>7</sup>, Helene Chepfer<sup>3</sup>, and Gregory Cesana<sup>3</sup>
<sup>1</sup>Cold and Arid Regions, Environmental and Engineering Research Institute, Chinese Academy of Sciences, Beijing, China,

<sup>2</sup>Key Laboratory of Tibetan Environment Changes and Land Surface Processes, Institute of Tibetan Plateau Research, Chinese Academy of Sciences, Beijing, China, <sup>3</sup>Laboratoire de Météorologie Dynamique, Institut Pierre Simon Laplace, CNRS, Paris, France, <sup>4</sup>CAS Center for Excellence in Tibetan Plateau Earth Sciences, Chinese Academy of Sciences, Beijing, China, <sup>5</sup>Laboratoire des Sciences du Climat et de l'Environnement /Institut Pierre Simon Laplace (UMR CEA CNRS UVSQ 8212), Gif-sur-Yvette, France, <sup>6</sup>Department of Biology, San Diego State University, San Diego, California, USA,

<sup>7</sup>Jet Propulsion Laboratory, California Institute of Technology, Pasadena, California, USA,

**Abstract** Precipitation isotopologues recorded in natural archives from the southern Tibetan Plateau may document past variations of Indian monsoon intensity. The exact processes controlling the variability of precipitation isotopologue composition must therefore first be deciphered and understood. This study investigates how atmospheric convection affects the summer variability of  $\delta^{18}\text{O}$  in precipitation ( $\delta^{18}\text{O}_p$ ) and  $\delta\text{D}$  in water vapor ( $\delta\text{D}_v$ ) at the daily scale. This is achieved using isotopic data from precipitation samples at Lhasa, isotopic measurements of water vapor retrieved from satellites (Tropospheric Emission Spectrometer (TES), GOSAT) and atmospheric general circulation modeling. We reveal that both  $\delta^{18}\text{O}_p$  and  $\delta\text{D}_v$  at Lhasa are well correlated with upstream convective activity, especially above northern India. First, during days of strong convection, northern India surface air contains large amounts of vapor with relatively low  $\delta\text{D}_v$ . Second, when this low- $\delta\text{D}_v$  moisture is uplifted toward southern Tibet, this initial depletion in HDO is further amplified by Rayleigh distillation as the vapor moves over the Himalayan. The intraseasonal variability of the isotopologue composition of vapor and precipitation over the southern Tibetan Plateau results from these processes occurring during air mass transportation.

## 1. Introduction

The isotopologues of precipitation ( $\text{HDO}$  and  $\text{H}_2^{18}\text{O}$ ) stored in natural archives have long been used for paleoclimate reconstructions [Dansgaard et al., 1969; Jouzel et al., 1987; Yao et al., 1996]. The Tibetan Plateau (TP) and its surrounding areas contain the largest number of glaciers outside polar regions, from which ice cores can be extracted and analyzed. However, the exact climatic controls on the isotopologue composition of precipitation on the TP remain debated. This makes the climatic interpretation of isotopologue variations recorded in Tibetan ice cores and other archives uncertain at interannual, decadal, or paleoclimatic time scales.

The relative abundances of isotopologues in water samples are quantified by the equation:  $\delta = 1000 \times (R_{\text{sample}}/R_{\text{VSMOW}} - 1)$  and they are expressed in per mil.  $R_{\text{sample}}$  is the abundance ratio of the heavy to light isotopologue in a sample, and  $R_{\text{VSMOW}}$  is the abundance ratio of the heavy to light isotopologue in VSMOW water (Vienna standard mean ocean water). VSMOW is characterized by a  $D/H$  ratio of  $155.76 \times 10^{-6}$  and a  $^{18}\text{O}/^{16}\text{O}$  ratio of  $2005.2 \times 10^{-6}$ .

Several factors can affect the isotopologue composition of water vapor and precipitation over the TP. The “temperature effect,” i.e., a positive local correlation between temperature and heavy isotopologue composition in precipitation ( $\delta^{18}\text{O}_p$ ), has been widely documented, especially in the northern TP [Yao et al., 1996; Tian et al., 2001a; Yu et al., 2008], and early interpretations of Tibetan ice cores were focused on temperature [Thompson, 2000]. In the southern part of the TP, in contrast, the “amount effect,” i.e., a negative correlation

between local precipitation amount and  $\delta^{18}\text{O}_p$ , has been documented [Tian, 2003]. Relationships with precipitation amount can also be nonlocal and involve upstream effects. Several studies have highlighted the important role of convective activity along air mass trajectories in various monsoon regions: Asia [Vuille *et al.*, 2005; Schmidt *et al.*, 2007; LeGrande *et al.*, 2009; Lee *et al.*, 2012; Gao *et al.*, 2013], Western Africa [Risi *et al.*, 2008a, 2008b; Tremoy *et al.*, 2012] and South America [Vimeux *et al.*, 2005, 2011; Samuels-Crow *et al.*, 2014]. Moreover, changes in moisture sources and transport paths are also known to affect TP precipitation isotopologue composition [Araguas-Araguas *et al.*, 1998; Aggarwal *et al.*, 2004; Jouzel *et al.*, 2013], and specifically the relative contributions of moisture transported by westerlies or Indian monsoon flow [Yao *et al.*, 2013].

The goal of this study is to better understand what controls the isotopologue composition of precipitation recorded in Southern Tibetan ice cores. As a first step, we focus here on understanding the climatic controls on  $\delta^{18}\text{O}_p$  at the daily scale. We expect isotopologue variations at the daily scale to reflect atmospheric processes in a more straightforward way than at longer time scales. The signal archived in ice cores arises from the accumulation of precipitating events which therefore integrate synoptic or intraseasonal phenomena. Lhasa (29.70°N, 91.13°E), where continuous and long-term precipitation isotopologue composition ( $\delta^{18}\text{O}_p$ ) monitoring has been operational since 1996 [Tian *et al.*, 2001a; Tian, 2003; Gao *et al.*, 2011, 2013; Yao *et al.*, 2013], was selected as a representative site of the southern TP where summer (June–July–August–September; JJAS) climate is primarily under the influence of the Indian summer monsoon [Yao *et al.*, 2012; Mölg *et al.*, 2014]. Understanding the processes controlling the variability of Lhasa precipitation isotopologue composition may also shed new light on the interpretation of nearby ice core records, such as those drilled at Zhadang (30.50°N, 90.65°E) and Gurenhejou (30.19°N, 90.46°E) [Yu *et al.*, 2013]. A recent classification of TP glaciers based on very high-resolution reanalysis products and calculation of seasonality of precipitation/accumulation concludes that glaciers from south to central Tibet, near Lhasa are unequivocally dominated by summer precipitation (more than 60% from JJA) [Fabien *et al.*, 2014]. Lhasa is located at an elevation of 3685 m above sea level, with an average summer temperature of 12°C. We focus here on the summer season, from June to September, which accounts for 85% of annual southern TP precipitation [Yao *et al.*, 2012]. The annual mean precipitation amount is 400 mm from 1997 to 2007.

Precipitation samples at Lhasa were collected at event scale during 3 years (2005–2007). Statistical analyses of this data set revealed that the intrasummer variability of Lhasa  $\delta^{18}\text{O}_p$  is closely related to the variability of upstream convection in northern India, several days prior to the precipitation event [Gao *et al.*, 2013]. Here in order to understand the mechanisms relating upstream convection and  $\delta^{18}\text{O}_p$ , we complement this data set with remote sensing data which allow us to investigate the evolution of water vapor isotopologue composition ( $\delta\text{D}_v$ ) along air mass trajectories. The isotopologue composition of water vapor provides key information: (1) vapor is observed more continuously in space and time than precipitation, which is only sampled during precipitation events; (2) unlike precipitation, it is less affected by postcondensational processes such as reevaporation of falling droplets [Risi *et al.*, 2008b, 2010a; Lee and Fung, 2008]; (3) analyzing vapor isotopologue composition along trajectories allows us to understand how different processes progressively affect its composition. Remote sensing observations of  $\delta\text{D}_v$  also offer unrivaled spatial and temporal coverage [Worden *et al.*, 2007; Frankenberg *et al.*, 2009, 2013a; Lacour *et al.*, 2012]. In this paper, we use both Tropospheric Emission Spectrometer (TES) data [Worden *et al.*, 2007, 2012] and Greenhouse Gases Observing Satellite (GOSAT) data [Frankenberg *et al.*, 2013a], two sources of information with different retrieval methodologies, to assess robust findings.

The water vapor isotopologues are highly influenced by cloud processes, during which precipitation is formed and isotopic fractionation occurs. In convection regions, the detrainment from convective clouds plays an important role on the isotopologue composition of water vapor [Moyer *et al.*, 1996; Risi *et al.*, 2012]. We also use the Cloud-Aerosol lidar and Infrared Pathfinder Satellite Observation (CALIPSO) to characterize the vertical profiles of cloud cover [Winker *et al.*, 2007], to help understand the vertical profiles of water vapor isotopologue composition.

To better understand the processes controlling the  $\delta\text{D}_v$  and  $\delta^{18}\text{O}_p$  at Lhasa, an atmospheric general circulation model (GCM) is used. LMDZ is a general circulation model (GCM) developed at Laboratoire de Météorologie Dynamique (LMD) [Hourdin *et al.*, 2006]. An isotopic version (hereafter LMDZiso) has been developed [Risi *et al.*, 2010b]. Here we take advantage of the LMDZ GCM which has a zoom functionality [Krinner *et al.*, 1997; Coindreau *et al.*, 2007]. Its stretched grid provides increased horizontal resolution down to a few tens

of kilometers, allowing us to focus on a specific region. Such enhanced resolution is particularly useful for mountainous regions such as the southern TP [Yao *et al.*, 2013]. Here the isotopic measurements are also used to investigate the performance of different model versions, which include different physical packages for the representation of convection.

We describe the data sets and model simulations in section 2. In section 3, the isotopologue composition of precipitation and vapor simulated by LMDZiso are compared with observations. The links between  $\delta^{18}\text{O}_p$ ,  $\delta\text{D}_v$ , convective activity and air mass trajectories are investigated. In section 4, the evolution of water vapor isotopologue composition along the trajectories to Lhasa is analyzed in more detail. Section 5 summarizes our results and perspectives on future work.

## 2. Data and Methods

### 2.1. In Situ Measurements

Precipitation samples were collected at Lhasa from 2005 to 2007 at the event scale. All  $\delta^{18}\text{O}_p$  samples were measured using a MAT-253 mass spectrometer with an analytical precision of 0.05‰ in the Key Laboratory of CAS (Chinese Academy of Sciences). All the data were calibrated with respect to VSMOW. Altogether, 294 precipitation events were sampled with information on precipitation  $\delta^{18}\text{O}_p$ , precipitation amount, and surface air temperature. Only the events that occurred in JJAS (200 out of 294 events) will be discussed in the paper. If several events occurred on the same day, observations were lumped into one single event, and the total daily precipitation amount, the average temperature, and the precipitation weighted  $\delta^{18}\text{O}_p$  were calculated before comparing to daily mean data in LMDZiso.

### 2.2. TES

TES instrument on board on the Aura satellite is a nadir-viewing infrared Fourier transform spectrometer from which the deuterium content of water vapor ( $\delta\text{D}_v$ ) can be retrieved [Worden *et al.*, 2004; Worden *et al.*, 2006, 2007]. The footprint of each nadir observation is 5.3 km  $\times$  8.5 km. Its precision is about 10‰–15‰ for individual measurement but uncertainty is reduced by averaging several measurements [Worden *et al.*, 2006; Risi *et al.*, 2013]. The original  $\delta\text{D}_v$  retrievals were most sensitive around 600 hPa [Worden *et al.*, 2006]. A new processing leads to  $\delta\text{D}_v$  retrievals with enhanced vertical sensitivity from 925 hPa to 450 hPa in the tropics and at high latitudes during summer. The sensitivity of the retrievals and their uncertainties may depend on altitude [Worden *et al.*, 2012]. This may affect the absolute values but is less likely to affect the temporal variability. Therefore, when interpreting TES retrievals, we focus on temporal variability rather than on absolute values. To check that the sensitivity effects are not driving some variability patterns, we systematically compare model outputs before and after applying averaging kernels. The degree of freedom of the signal is 1.8 on average over the tropics, meaning that vertical profiles bear information on more than one level. For example, profiles with a degree of freedom of 3 bear information on three independent levels. Here we use the vertical profiles retrieved by TES from 2005 to 2007 when in situ precipitation samples were collected at Lhasa. We select only measurements for which the quality flag is set to unity and for which the degree of freedom of the signal is higher than 0.5 [Risi *et al.*, 2013]. Over 366 JJAS days, the quality selection leaves us with 122 days of valid TES measurements.

### 2.3. GOSAT

GOSAT was launched to monitor the atmospheric concentrations of carbon dioxide and methane. GOSAT measurements also enable retrieval of the total column water vapor content in HDO and  $\text{H}_2\text{O}$  [Frankenberg *et al.*, 2013b]. Column-integrated  $\delta\text{D}_v$  is strongly weighted toward the  $\delta\text{D}_v$  of the boundary layer where water vapor is most abundant [Frankenberg *et al.*, 2009]. The  $\delta\text{D}_v$  in GOSAT are thus mainly sensitive to lower atmosphere levels. The topography has a strong impact on GOSAT's column-integrated  $\delta\text{D}_v$ . The total column in Northern India represents mainly the lower troposphere, whereas over the TP it represents the midtroposphere. GOSAT was not launched until 23 January 2009; there is no overlap with Lhasa precipitation data. Here we use GOSAT measurements in JJAS from 2009 to 2011 [Frankenberg *et al.*, 2009, 2013a] when LMDZiso simulations are also available. The precision of GOSAT measurement is about 20‰–40‰, and we can increase precision by averaging several measurements [Risi *et al.*, 2013].

We select only GOSAT measurements that met several quality criteria. Scenes identified as cloudy by the GOSAT retrieval algorithm are screened out [Frankenberg *et al.*, 2013a]. Retrieved precipitable water must agree within 30% with ERA-40 reanalysis. Errors on retrieved precipitable water and column-integrated HDO

must be lower than 15% [Frankenberg *et al.*, 2013a]. Retrieved  $\delta D_v$  must be between  $-900\text{‰}$  and  $1000\text{‰}$  to exclude a few physically unrealistic values. Over 366 JJAS days, the quality selection leaves us with 49 days of valid GOSAT measurements.

Two kinds of sampling biases may affect TES and GOSAT observations. First, there is a diurnal sampling effect. TES observations are generally retrieved at 01:30 and 13:30 local time (around 13:00 for GOSAT), while we used LMDZ results averaged at the daily scale. However, the high correlation ( $> 0.9$ ) between  $\delta D_v$  diurnal mean and  $\delta D_v$  at 01:30 and 13:30 local time in LMDZ indicates that it has no great impact on the comparison between remote sensing products and LMDZ results.

Second, there can be a “clear-sky” bias. TES and GOSAT retrievals are restricted to fields of view for which cloud fraction is relatively small. Again, using LMDZ results, we found that this bias has no significant impact on the comparison. The relationship between  $\delta D_v$  at Lhasa and convection in Northern India (which is the core of our paper, see sections 3 and 4) is similar when either using all days of JJAS or only clear-sky days (e.g., cloud fraction lower than 0.15). For example, in LMDZ, the daily correlation coefficients between  $\delta D_v$  at Lhasa at 500 hPa and outgoing longwave radiation (OLR) in Northern India 3 days prior are 0.35 ( $p < 0.05$ ) and 0.30 ( $p < 0.05$ ), respectively, when using all days of JJAS or only clear-sky days.

#### 2.4. Convection and Cloud Data Set

The daily NOAA OLR product from 2005 to 2011, with a resolution of  $2.5^\circ \times 2.5^\circ$ , is used here as an index of tropical convection [Liebmann and Smith, 1996]. Lower OLR values correspond to lower cloud temperature and thus higher cloud top height, which is a signature of the convection. For example, OLR values lower than 220 or 240 W/m<sup>2</sup> are often identified as deep convection [Zhang, 1993; Fu *et al.*, 1990]. Details on the threshold used here to identify convection days will be discussed in section 4.1. For precipitation, we use the Global Precipitation Climatology Project (GPCP) data [Huffman *et al.*, 2001] at daily scale, with a spatial resolution of  $1^\circ \times 1^\circ$ .

For cloudiness, we use the GCM-Oriented CALIPSO Cloud Product (CALIPSO-GOCCP) [Chepfer *et al.*, 2010]), which has been designed to evaluate clouds in GCMs. CALIPSO-GOCCP data set provides information on the 3-D distribution of clouds. Its vertical resolution is 480 m from 0 km to 19.2 km altitude with profiles every 333 m along the satellite track. As for TES and GOSAT, we use a model-to-satellite approach to compare observations and the model. More specifically, we compare CALIPSO-GOCCP data set and LMDZ outputs with the lidar simulator [Chepfer *et al.*, 2008; Bodas-Salcedo *et al.*, 2011], which uses definition of clouds and sampling consistent with CALIPSO-GOCCP data set.

#### 2.5. Back Trajectories

We calculate air mass back trajectories using the Hybrid Single-Particle Lagrangian Integrated Trajectory (HYSPPLIT) model [Draxler, 1998]. In order to describe the airflow reaching Lhasa at 1000 m AGL (above ground level), in our study, back trajectories at 6 h time steps 5 days prior to arrival in Lhasa were computed from 2005 to 2007 when TES data were available. National Centers for Environmental Prediction (NCEP) reanalysis data were used (<ftp://arlftp.arl.hq.noaa.gov/pub/archives/reanalysis/>). The back trajectories are sensitive to uncertainties in the reanalysis data set. Different reanalysis data sets may lead to different performance on Tibet for humidity and precipitation, but similar skills are reported for horizontal winds [Wang and Zeng, 2012; Bao *et al.*, 2013].

#### 2.6. LMDZiso GCM

Here LMDZ is forced by observed sea surface temperature (SST) and sea ice following the Atmospheric Model Intercomparison Project protocol [Gates, 1992]. The simulation is nudged to the three-dimensional horizontal winds from European Centre for Medium-Range Weather Forecasts operational analyses [Klinker *et al.*, 2000]. The land surface scheme in LMDZiso is a simple bucket in which no distinction is made between bare soil evaporation and transpiration, and no fractionation is considered during evapotranspiration [Risi *et al.*, 2010b]. We compare the data simulated by LMDZiso from 2005 to 2007 with the in situ measurements at Lhasa, and from 2009 to 2011 with the GOSAT retrievals.

When we compare LMDZiso simulations to the TES or GOSAT data, we take into account the spatiotemporal sampling. For a rigorous model-data comparison, the sensitivity of the retrieval must also be taken into account. The averaging kernel matrix provided in the product defines the sensitivity of the retrieval at each

level to the true state at each level [Lee *et al.*, 2011; Risi *et al.*, 2012]. We thus apply the same averaging kernels used for the retrieval process to the LMDZiso simulations [Risi *et al.*, 2012], when comparing to both TES and GOSAT.

In order to assess the impact of the model resolution and physical package on the processes controlling TP water isotopologues, we have used three versions of LMDZiso: (1) LMDZiso Standard has a resolution of  $3.75^\circ \times 2.5^\circ$  and 19 vertical levels in the atmosphere; (2) LMDZiso Zoom has the same physics as LMDZiso Standard, but a refined horizontal resolution over the TP down to about 50 km, in a region spanning from about  $60^\circ\text{E}$  to  $130^\circ\text{E}$  in longitude and from  $0$  to  $50^\circ\text{N}$  in latitude; (3) LMDZiso NP (where NP stands for new physical package) has the same horizontal and vertical resolution as in LMDZiso Standard but includes a new boundary layer scheme and associated clouds, a cold pool scheme, and a new closure and triggering scheme for deep convection [Rio *et al.*, 2009; Grandpeix and Lafore, 2010; Rio *et al.*, 2013]. In LMDZ NP, the low-level and midlevel cloud cover is dramatically enhanced compared to LMDZ Standard in all regions including over the Indian Monsoon region, in better agreement with observations. The diurnal cycle of convective rainfall over continents is also shifted toward later times of day over all continental regions including the Asian Monsoon region, in better agreement with observations. However, the distribution of precipitation in the Asian Monsoon region remains essentially the same in LMDZ NP as in LMDZ Standard [Hourdin *et al.*, 2013].

### 3. Main Controls on Precipitation Isotopic Composition

#### 3.1. Seasonal Variations in Observed Precipitation Isotopologue Composition.

According to the daily evolution of  $\delta^{18}\text{O}_p$  and of precipitation amount over the 2005–2007 period,  $\delta^{18}\text{O}_p$  is lower during July–August when the Indian monsoon prevails, than in June and September when impact of the monsoon weakens. The weighted average  $\delta^{18}\text{O}_p$  in July is  $-18.14\text{‰} \pm 1.48\text{‰}$  and in August is  $-19.48\text{‰} \pm 2.69\text{‰}$  while weighted average  $\delta^{18}\text{O}_p$  in June is  $-8.25\text{‰} \pm 4.48\text{‰}$  and  $-16.96\text{‰} \pm 1.91\text{‰}$  in September.  $\delta\text{D}_p$  data are unavailable, but previous studies have demonstrated a strong correlation between  $\delta\text{D}_p$  and  $\delta^{18}\text{O}_p$  [Tian *et al.*, 2001b]. The average precipitation amount in July is  $105 \text{ mm} \pm 39 \text{ mm}$  and in August is  $126 \text{ mm} \pm 61 \text{ mm}$ , while precipitation amount in June is  $71 \text{ mm} \pm 8 \text{ mm}$  and in September is  $59 \text{ mm} \pm 15 \text{ mm}$ . However, this seasonality cannot be simply interpreted in terms of the local amount effect. For example,  $\delta^{18}\text{O}_p$  is higher in June than in September and the precipitation amount is also larger. Hereafter, we investigate what controls the daily variability in  $\delta^{18}\text{O}_p$ .

#### 3.2. Data-Model Comparison in Precipitation and in Vapor

Before using LMDZiso to investigate what controls  $\delta^{18}\text{O}_p$ , we evaluate its capacity to simulate the daily variability in  $\delta^{18}\text{O}_p$ .

LMDZiso was shown to reasonably capture the variability of southern TP  $\delta^{18}\text{O}_p$  at the event and seasonal scales [Gao *et al.*, 2011]. Their study showed that the high-resolution simulation performed with LMDZiso Zoom produces more realistic daily and monthly variations in  $\delta^{18}\text{O}_p$  at Lhasa than LMDZiso Standard. Here we analyze this capacity in more detail by comparing three versions of LMDZiso with in situ and satellite data at Lhasa, focusing on the daily scale in JJAS. This comparison is performed for periods when both simulated and observed data are available, which differs for each source of information.

All versions of LMDZiso reasonably represent the relationship between precipitation amount and  $\delta^{18}\text{O}_p$  (Figure 1a). At the daily scale, the Pearson correlation coefficients between the observed and simulated  $\delta^{18}\text{O}_p$  are, respectively, 0.46 for LMDZiso Standard, 0.33 for LMDZiso NP, and 0.58 for LMDZiso Zoom in Figure 1b. Note that LMDZiso Zoom, with the highest horizontal resolution, can reasonably reproduce both the patterns and absolute values of  $\delta^{18}\text{O}_p$  in Lhasa. The weighted average JJAS  $\delta^{18}\text{O}_p$  is  $-16.54\text{‰} \pm 7.31\text{‰}$  in the observations and  $-16.35\text{‰} \pm 4.70\text{‰}$  in LMDZiso Zoom. By contrast, LMDZiso Standard and NP produce much higher  $\delta^{18}\text{O}_p$  values ( $-10.51\text{‰} \pm 3.43\text{‰}$  and  $-6.62\text{‰} \pm 3.20\text{‰}$  respectively), which may be due to the coarse representation of the topography. For the simulation of precipitation, LMDZiso Standard reasonably reproduces the mean JJAS precipitation amount ( $400 \text{ mm} \pm 94 \text{ mm}$ , against  $360 \text{ mm} \pm 108 \text{ mm}$  in the observations). By contrast, LMDZiso Zoom underestimates the precipitation amount at Lhasa (only  $200 \text{ mm} \pm 99 \text{ mm}$ ) while LMDZiso NP overestimates observation ( $1000 \text{ mm} \pm 460 \text{ mm}$ ). The large standard deviation of precipitation in LMDZiso NP results from the large precipitation ( $1500 \text{ mm}$ ) in 2007 compared with precipitation in 2005 ( $770 \text{ mm}$ ) and in 2006 ( $750 \text{ mm}$ ).



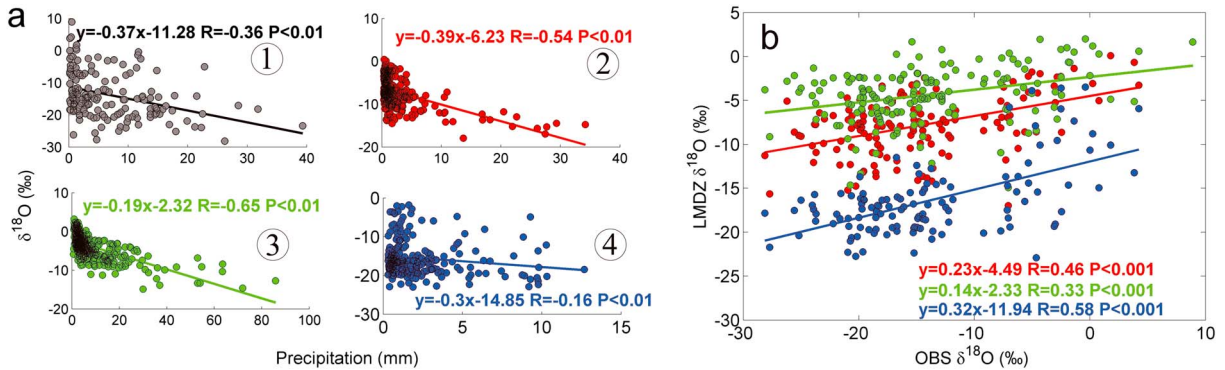


**Figure 1.** The regressions of  $\delta^{18}O_p$  with daily precipitation amount (a) in JJAS from 2005 to 2007. The numbers 1, 2, 3, 4 represent the observation (black), LMDZiso Standard (red), NP version (green) and Zoom (blue) and (b) the comparison of  $\delta^{18}O_p$  at Lhasa between observation and simulations.

For visibility and simplicity, sometimes only the results for the standard version are shown, but we discuss whenever the three versions give different results. Figure 2 compares the observed and simulated atmospheric water vapor amount and  $\delta D_v$  in LMDZiso. Compared with TES data, LMDZiso Standard can reasonably reproduce the  $q$ - $\delta D_v$  diagram, daily  $\delta D_v$ , and  $q$  variability at 500 hPa (Figures 2a–2c). The comparison with GOSAT data set (Figures 2d–2f) also confirms LMDZiso's ability for capturing isotopologue variability. The correlation coefficients between GOSAT observations and simulations are 0.65 (precipitable water) and 0.41 ( $\delta D_v$ ), respectively. Table 1 summarizes the comparison between the three LMDZiso versions and satellite data. We note that none of the LMDZiso version perform unequivocally better than another and that there is no relationship between the model skills for local precipitation amount and for the isotopologue composition of vapor and precipitation. Overall, the best performance is, for both averages and variability, obtained using Zoom version, consistent with previous studies [Gao et al., 2011; Yao et al., 2013], though it does not reasonably reproduce the isotopologue content retrieved from GOSAT.

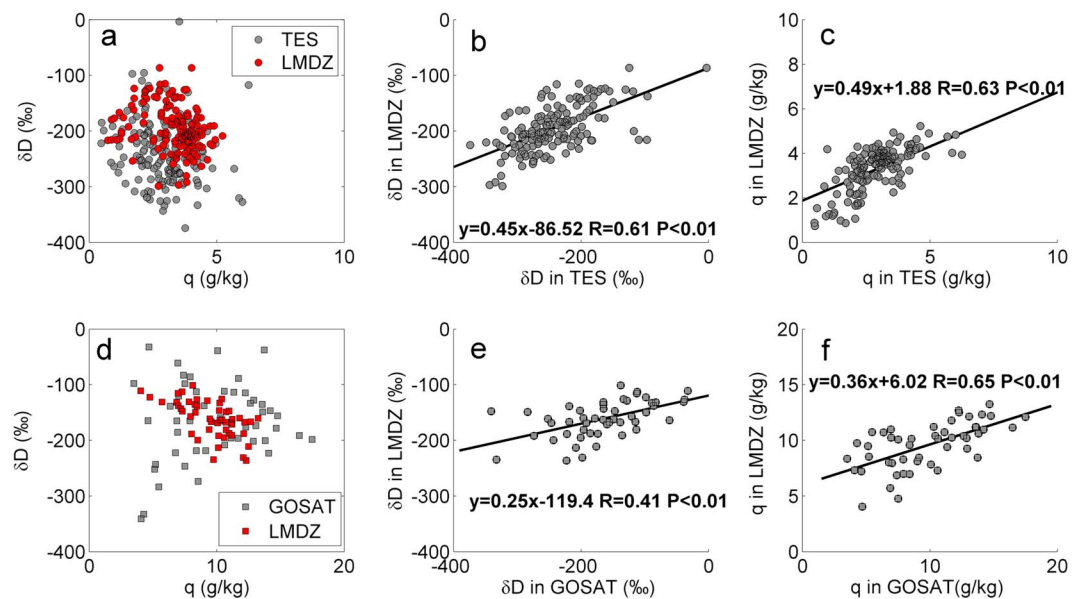


**Figure 2.** (a–c) Comparison of  $q$  and  $\delta D_v$  properties between the LMDZiso Standard simulation and the TES observations at 500 hPa at Lhasa, for all months from 2005 to 2007: Figure 2a shows  $q$  –  $\delta D_v$  diagram retrieved from TES and simulated by LMDZiso, Figure 2b shows  $\delta D_v$ , and Figure 2c shows  $q$  simulated by LMDZiso as a function of the corresponding values retrieved from TES. (d–f) Same as Figures 2a–2c but comparing the precipitable water and total column  $\delta D_v$  between the LMDZiso Standard simulation and the GOSAT observations. LMDZiso outputs were collocated with the TES or GOSAT data sets and applied the corresponding averaging kernels.

**Table 1.** Mean  $\delta D_v$  and  $q$ , and Corresponding Standard Deviation at 500 hPa (TES/LMDZiso) or Integrated Over the Total Column (GOSAT/LMDZiso) Over Lhasa in JJAS<sup>a</sup>

	Statistics	Observation	Standard	NP	Zoom
TES	Mean $\delta D_v$	−242 ‰	−194 ‰	−185 ‰	−243 ‰
	SD $\delta D_v$	57 ‰	41 ‰	42 ‰	45 ‰
	r	1.0	0.61	0.44	0.67
	Mean $q$	2.9 g/kg	3.3 g/kg	3.9 g/kg	3.7 g/kg
	SD $q$	1.2 g/kg	0.96 g/kg	0.76 g/kg	0.68 g/kg
GOSAT	r	1.0	0.63	0.52	0.51
	Mean $\delta D_v$	−165 ‰	−209 ‰	−177 ‰	−349 ‰
	SD $\delta D_v$	34 ‰	36 ‰	38 ‰	45 ‰
	r	1.0	0.41	0.40	0.31
	Mean $q$	9.8 g/kg	9.6 g/kg	13.4 g/kg	13.1 g/kg
In situ	SD $q$	3.6 g/kg	2.1 g/kg	1.8 g/kg	1.3 g/kg
	r	1.0	0.65	0.46	0.21
	Mean $\delta^{18}O_p$	−16.54 ‰	−10.51 ‰	−6.62 ‰	−16.35 ‰
	SD $\delta^{18}O_p$	7.31 ‰	3.43 ‰	3.20 ‰	4.70 ‰
	r	1.0	0.46	0.33	0.58

<sup>a</sup>Mean  $\delta^{18}O_p$  and corresponding standard deviation at Lhasa(Observation/LMDZiso). The Standard, NP, Zoom represent the different versions of LMDZiso. We report the Pearson's correlation coefficient between observations and LMDZiso.

LMDZiso produced a similar strength of correlation between  $\delta D_v$  and  $\delta^{18}O_p$ , with correlation coefficients of 0.47 (Figure 3b) for LMDZiso Standard, 0.46 ( $p < 0.01$ ) for LMDZiso NP and 0.56 ( $p < 0.01$ ) for LMDZiso Zoom (figure not shown).

To summarize, this model-data comparison shows that LMDZiso is able to capture a significant fraction of the observed intraseasonal variability for both  $\delta^{18}O_p$  and  $\delta D_v$  at Lhasa. In the following sections, we therefore use LMDZiso to better understand the drivers of this isotopologue variability.

### 3.3. Link Between $\delta^{18}O_p$ and $\delta D_v$ at Lhasa

To assess whether satellite  $\delta D_v$  are suitable for investigating the controls of  $\delta^{18}O_p$  at Lhasa, we show the relationship between  $\delta D_v$  and  $\delta^{18}O_p$  in Figure 3. The correlation coefficient between daily  $\delta^{18}O_p$  observed at Lhasa and local TES  $\delta D_v$  at 500 hPa is 0.43 ( $p < 0.01$ ). This correlation can be explained by two factors. First,  $\delta D_p$  and  $\delta D_v$  are tightly correlated. Second,  $\delta^{18}O_p$  is significantly and positively correlated with  $\delta D_p$ . In LMDZiso outputs, the correlation coefficient between daily summer variations of  $\delta^{18}O_p$  and  $\delta D_p$  at Lhasa is 0.99.

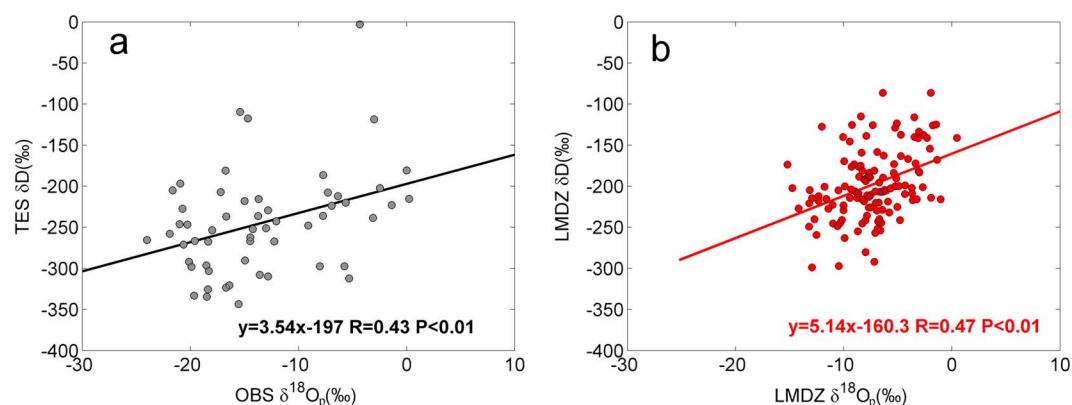


**Figure 3.** The relationship between  $\delta^{18}O_p$  and  $\delta D_v$  at Lhasa. (a) Observed  $\delta^{18}O_p$  and  $\delta D_v$  in TES at 500 hPa at Lhasa. (b) Same as Figure 3a but simulated by LMDZiso Standard.

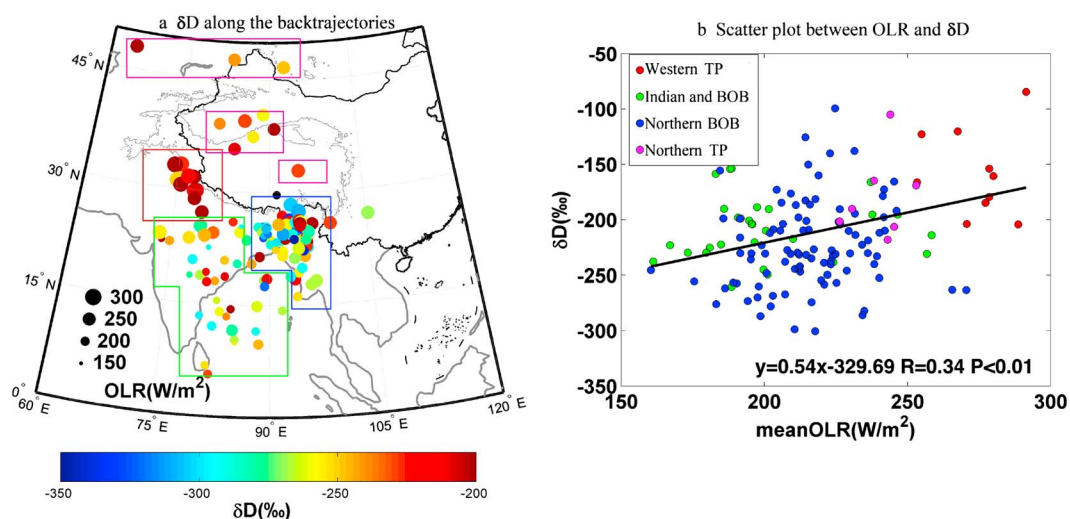


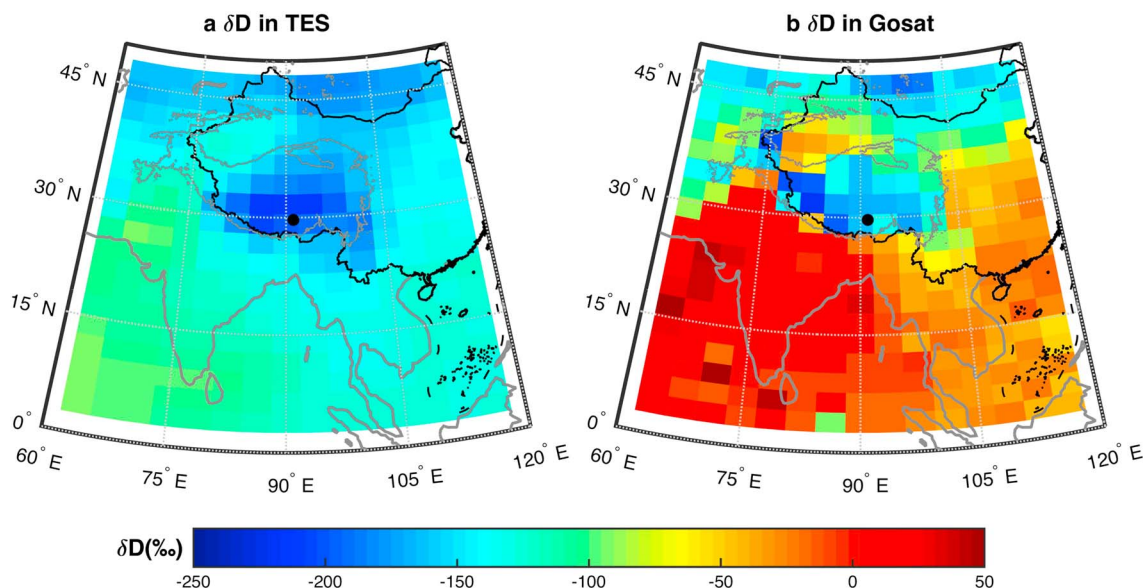
**Figure 4.** (a) Locations of air masses after 5 days along back trajectories from Lhasa. Back trajectories were launched for days when TES data were available over Lhasa in JJAS from 2005 to 2007. The circle color represents the  $\delta D_v$  at 500 hPa at Lhasa retrieved from TES, and the circle size represents the mean OLR along the back trajectories. (b)  $\delta D_v$  at Lhasa as a function of mean OLR along the back trajectories. The linear regression is also shown.

This means that LMDZiso simulates limited variations in deuterium excess at the daily scale. It is consistent with daily observations at Lhasa [Tian *et al.*, 2001b]. These findings indicate postcondensational do not significantly affect the variability of precipitation isotopologue composition.

Therefore, to understand the variability in the isotopologue composition of precipitation ( $\delta^{18}O_p$ ), we now focus on understanding the isotopologue composition of water vapor ( $\delta D_v$ ).

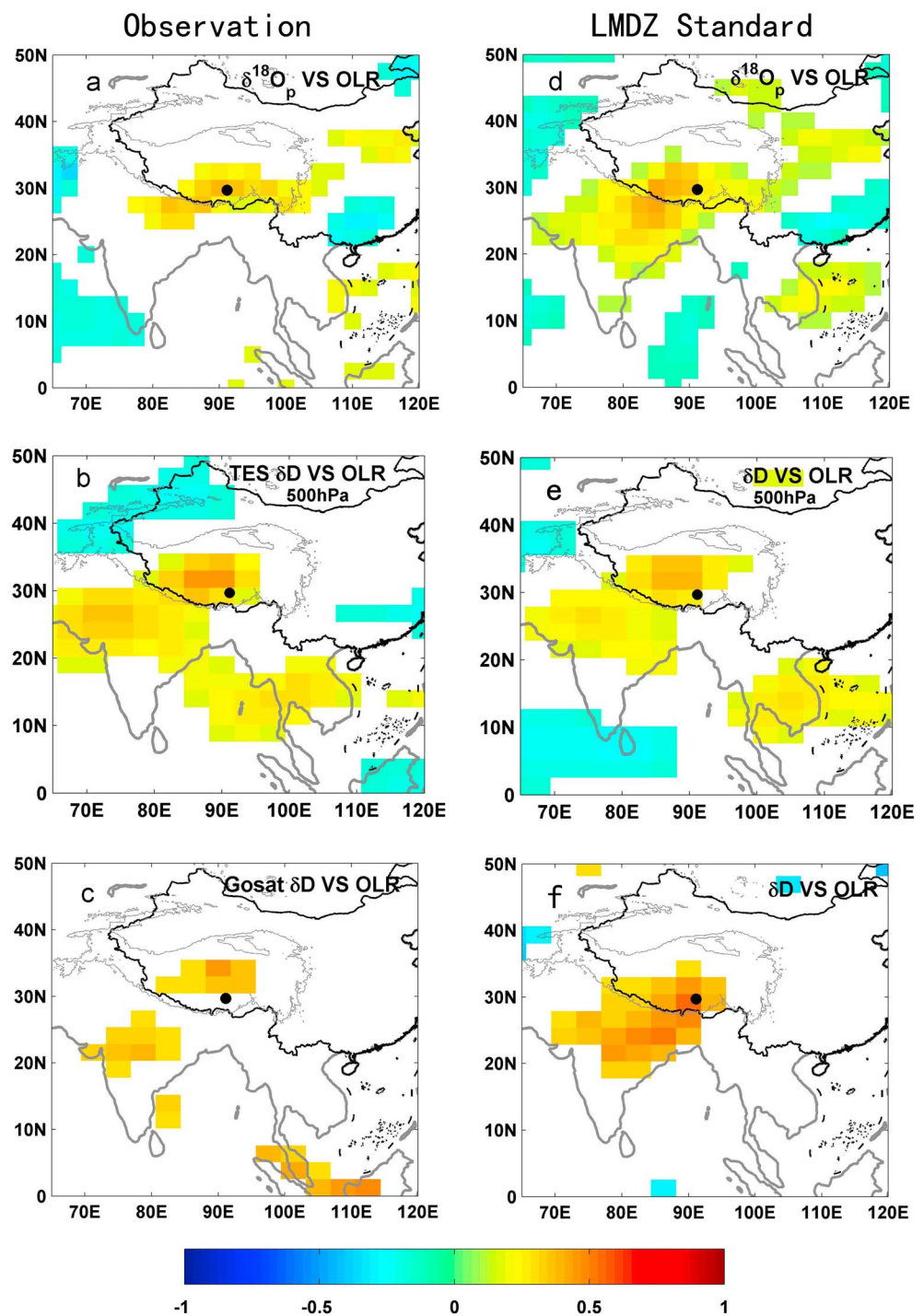
### 3.4. Relative Contribution of Moisture Source and of Convective Effects

Based on previous studies, the factors potentially controlling the  $\delta^{18}O_p$  of southern TP can be broadly classified into two effects: moisture source effects [Araguas-Araguas *et al.*, 1998; Tian *et al.*, 2001a; Tian, 2003; Yu *et al.*, 2008] and convective activity effects [Gao *et al.*, 2013]. Here we explore the relative importance of these two effects in JJAS combining  $\delta D_v$  from TES, HYSPLIT back trajectories, and OLR data.



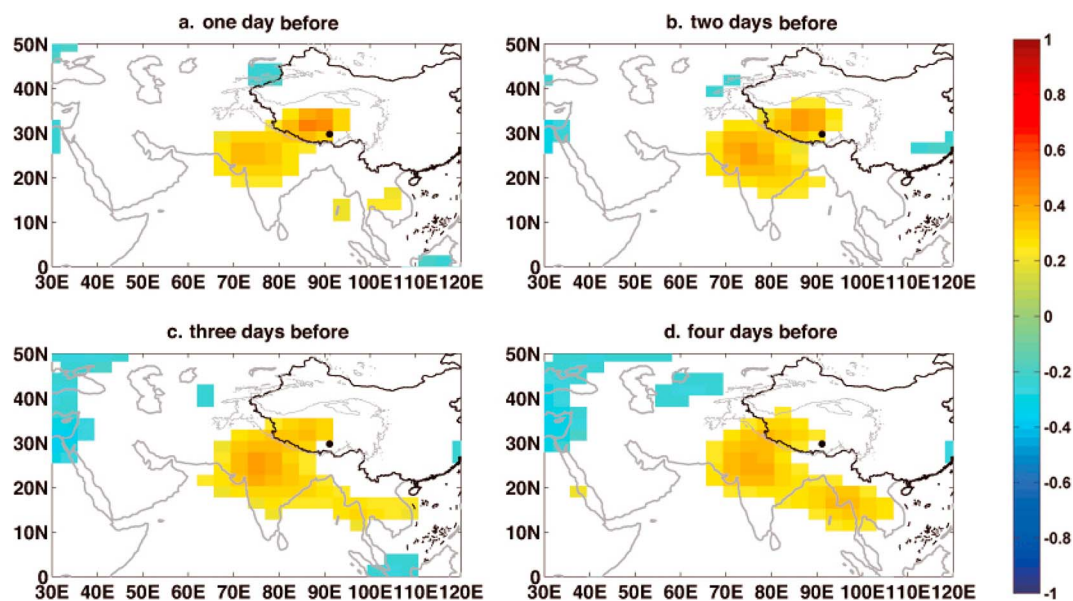
**Figure 5.** Spatial patterns of mean JJAS observed  $\delta D_v$ , from (a) TES (total column, 2005–2007) and (b) GOSAT (total column, 2009–2011). Note that for  $\delta D_v$ , calibration for satellite retrievals of  $\delta D_v$  values are not as reliable as observations of temporal and spatial variability.





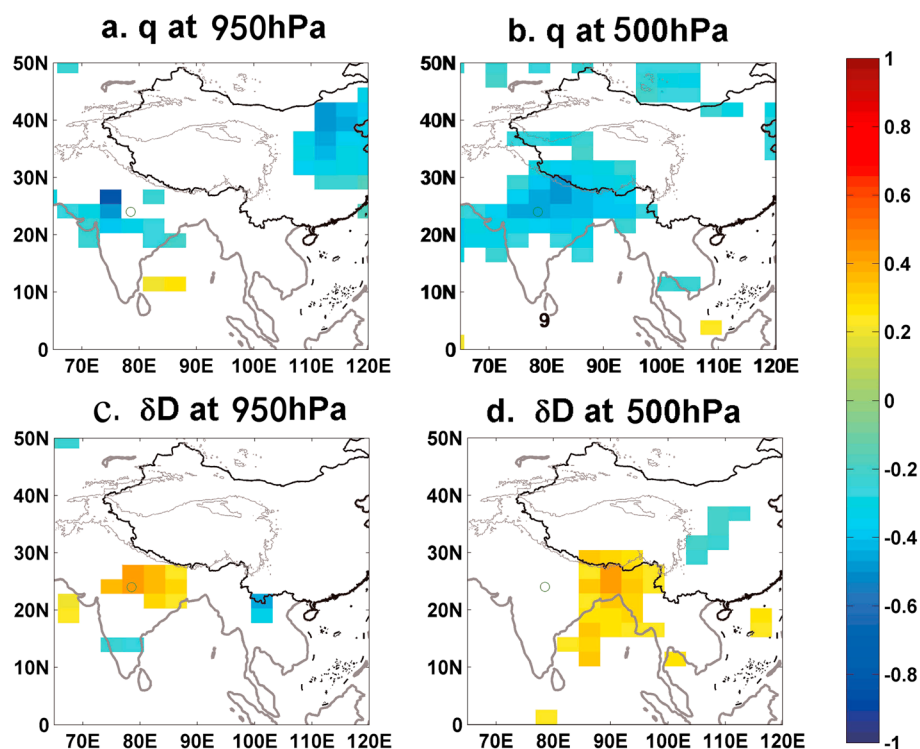
**Figure 6.** Daily correlation between the isotopologue composition ( $\delta^{18}\text{O}_p$  or  $\delta\text{D}_v$ ) at Lhasa and OLR, in JJAS. (a)  $\delta^{18}\text{O}_p$  at Lhasa. (b)  $\delta\text{D}_v$  from TES at 500 hPa. (c) Column-integrated  $\delta\text{D}_v$  from GOSAT. (d–f) Same as Figures 6a–6c but for LMDZiso Standard. These correlations are straight correlations without removal of the seasonality and insignificant correlations are masked.

Figure 4a shows the locations of the 5 day back trajectories, average OLR values over the 5 day trajectories, together with corresponding  $\delta\text{D}_v$  at Lhasa.  $\delta\text{D}_v$  is higher when trajectories come from the western (red box) and northern (pink box) TP than when they come from the south (green and blue boxes). However, Figure 4b also shows that this apparent moisture source effect may reflect a convective effect. The vapor with low  $\delta\text{D}$  values at Lhasa often transports over the regions with low OLR. This relationship holds for the



**Figure 7.** Daily correlations between  $\delta D_v$  from TES at 500 hPa over Lhasa and OLR in surrounding areas at time leads of (a) 1, (b) 2, (c) 3, and (d) 4 days. These correlations are straight correlations without removal of the seasonality and insignificant correlations are masked.

main source regions and for the whole set of trajectories.  $\delta D_v$  is higher over the south TP than over the northern TP (Figure 5). The low  $\delta D_v$  values in the northern TP could be due to large-scale mixing with extratropical water vapor sources with lower  $\delta D_v$  values [Galewsky and Hurley, 2010; Noone, 2012]. The  $\delta D_v$  spatial distribution contrasts with the fact that water vapor coming from the southern TP contains lower  $\delta D_v$  values at



**Figure 8.** Daily correlation between OLR in Northern India and specific humidity ( $q$ ), as retrieved from TES (a) at 950 hPa and (b) at 500 hPa. (c, d) Same as Figures 8a and 8b but for  $\delta D_v$  instead of  $q$ . These correlations are straight correlations without removal of the seasonality and insignificant correlations are masked.

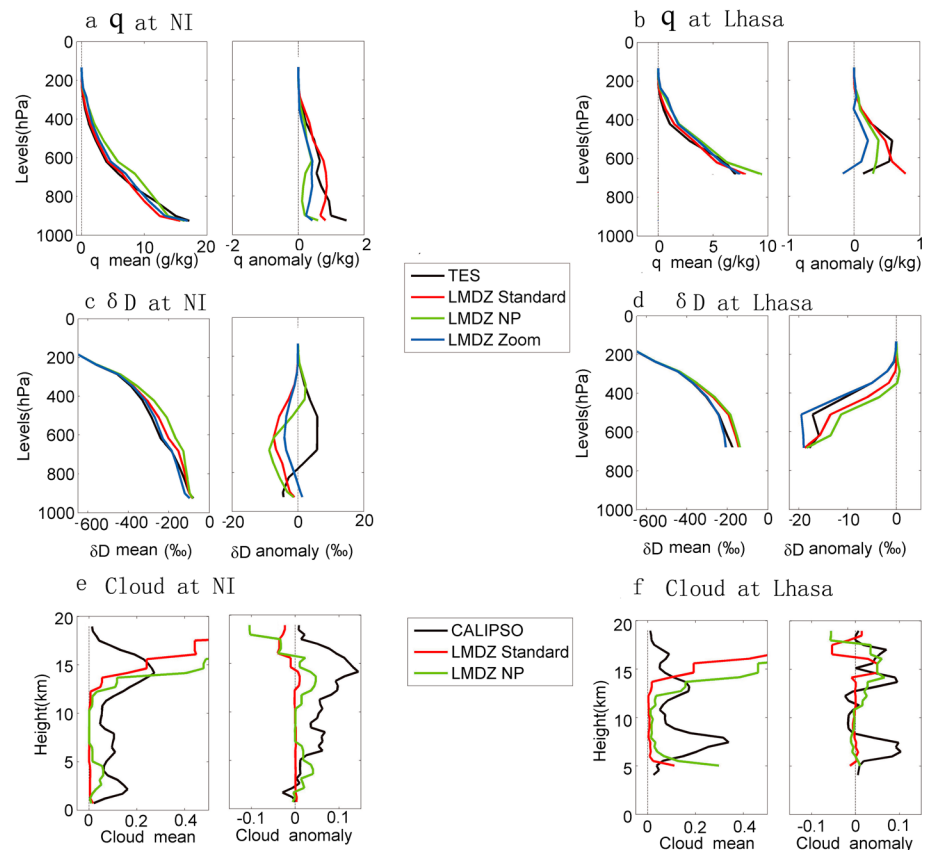


**Figure 9.** Profiles of  $q$ ,  $\delta D_v$ , and cloud cover both in NI and at Lhasa. (a, b) The profiles of  $q$  on average (JJAS mean conditions) and anomalies during LOW-OLR-NI conditions, in NI and at Lhasa, respectively, retrieved from TES and simulated by LMDZiso. Anomalies are calculated with respect to the JJAS mean values. LOW-OLR-NI conditions are defined as days of strong convection over NI (based on OLR data, see text) at the time when air masses over NI. The time lag associated with the duration of the transport from NI to Lhasa, which corresponds to several days, is estimated based on the back trajectory calculation. For example, if an air mass takes 4 days to travel from NI to Lhasa, then LOW-OLR-NI conditions are determined using OLR data 4 days before. (c, d) As in Figures 9a and 9b but for  $\delta D_v$ . (e, f) As in Figures 9a and 9b but for CALIPSO cloud fraction from 2006 to 2007. In each subfigure, the left panel represents the mean condition and the right panel the difference between strong convection days and the mean condition.

Lhasa than the vapor coming from the northern TP. This confirms that what mainly controls the  $\delta D_v$  at Lhasa at event scale in JJAS is not the  $\delta D_v$  at the moisture source, but rather how the initial  $\delta D_v$  is modified by convective activity along the trajectories toward Lhasa. The moisture source has only an indirect effect, depending on whether air masses go through convective regions or not. We therefore conclude that the relationship between convective activity and  $\delta D_v$  accounts for most of the relationship between moisture source and  $\delta D_v$  in JJAS.

### 3.5. Relationship Between Convection and Isotopologue Composition

The previous section points out the importance of convective activity in controlling  $\delta D_v$  at Lhasa. In this section, we investigate in detail the importance of local and upstream convection effects.

Figure 6 shows the spatial correlations between the isotopologue composition of precipitation and water vapor at different pressure levels over Lhasa and the regional OLR, based on observations and on simulations performed with LMDZiso Standard. The effect of convective activity on the isotopologue composition is similar for both  $\delta D_v$  (Figure 6) and  $\delta^{18}O_p$  [Gao *et al.*, 2013]. There is a significant positive correlation between vapor (or precipitation) isotopologue abundance at Lhasa and OLR at the regional scale (NI and around Lhasa). The correlation pattern is consistent across different levels (500 hPa and total column) in all data sets (in situ precipitation, TES and GOSAT).

The temporal evolution of the relationship between  $\delta D_v$  at 500 hPa at Lhasa and pre-Lhasa convective activity (1–4 days earlier) through NI is shown in Figure 7. As we go backward in time, this correlation coefficient at

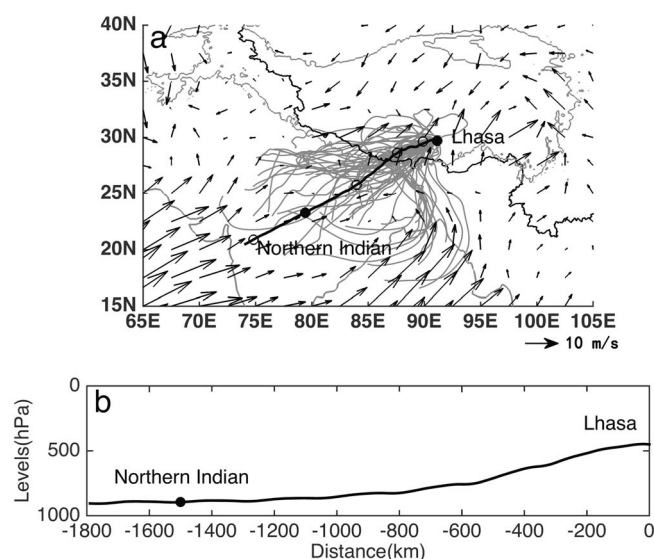


**Figure 10.** (a) JJAS mean wind vectors at 850 hPa from NCEP data set, 5 days back trajectories and mean back trajectory at Lhasa, (b) the altitude of mean trajectory at Lhasa. The circles represent locations for each of the 5 days along the trajectory.

that  $\delta D_v$  variations at Lhasa record changes in upstream convection, especially for those events that occurred in NI.

LMDZiso Standard reasonably simulates these correlation patterns (Figures 6d–6f) and their evolution through time (not shown). Similar results are obtained with LMDZiso Zoom and LMDZiso NP (not shown). This increases our confidence in using LMDZiso to study the link between NI convection and  $\delta D_v$ .

#### 4. How Does Deep Convective Activity Impact Vapor Isotopologue Composition?

Here we first investigate how deep convection affects  $\delta D_v$  in NI, and then inquire how the follow-up processes during transport affect  $\delta D_v$  at Lhasa. We define the center of NI as the point located at 24°N and 78.5°E, because this is where we find the highest correlation, outside of the TP, between OLR and  $\delta D_v$  in Lhasa (Figure 6). Convective activity in this region is also a useful indicator of the strength of the Asian monsoon [Wang and Fan, 1999].

##### 4.1. Influence of Convection in NI on Local Water Vapor $\delta D_v$

Figure 8 shows the relationship between OLR in NI, specific humidity, and  $\delta D_v$  at different pressure levels. At 950 hPa, anticorrelation between OLR and  $q$  in NI (Figure 8a) arises because intense convection tends to occur when low-level  $q$  is high [Holloway and Neelin, 2010]. The positive correlation between OLR and  $\delta D_v$  at 950 hPa (Figure 8c) likely results from the impact of unsaturated downdrafts, which are enhanced with convective activity, reducing the low-level  $\delta D_v$  [Risi et al., 2008a, 2010a]. Processes such as rain evaporation, rain-vapor exchanges, and moisture convergence can also contribute to reduced low-level  $\delta D_v$  [Lawrence et al., 2004; Worden et al., 2007; Risi et al., 2008a; Brown et al., 2008; Moore et al., 2014]. In the middle and upper troposphere, low OLR is associated with moister air (Figure 8b), which could be due to the moistening effect of convective detrainment. In NI, there is no obvious local correlation between OLR and  $\delta D_v$  in the middle and upper troposphere (Figure 8d).

The positive correlation between OLR in NI and  $\delta D_v$  in BOB may well arise from the northwestward propagation of monsoon depressions [Rajamani and Sikdar, 1989; Goswami, 2005]. Along the track of monsoon depressions, the rainfall region shifts from BOB to NI. Strong convection over NI is also associated with stronger-than-normal convection over BOB. The daily correlation coefficient is 0.5 between OLR in NI and OLR above BOB in JJAS. In BOB, strong convective activity is related to low  $\delta D_v$  at middle and upper atmospheric levels.

We conclude that convection in NI leads to decreases in low-level  $\delta D_v$  locally, and consequently affects  $\delta D_v$  at Lhasa 3–4 days later. How the convection in NI affects  $\delta D_v$  in middle and upper troposphere needs to be

NI increases from 0.30 (1 day earlier) to 0.35 (3 days earlier). Concurrently, the correlation between  $\delta D_v$  and OLR at Lhasa decreases. The pattern of relationships corresponds to the tracks of monsoon depressions that generate in the Bay of Bengal (BOB) (located at 10°N–20°N and 80°E–100°E) and migrate northwest over NI [Rajamani and Sikdar, 1989]. Such concurrencies indicate the potential value of  $\delta D_v$  in capturing signals of Indian monsoon processes. Similar results are obtained with GOSAT data (not shown). Thus, water vapor  $\delta D_v$  at Lhasa is more dependent on convection at the regional scale than at the local scale, consistent with previous studies based on either precipitation data or modeling [Gao et al., 2013; Schmidt et al., 2007; LeGrande et al., 2009]. These findings suggest



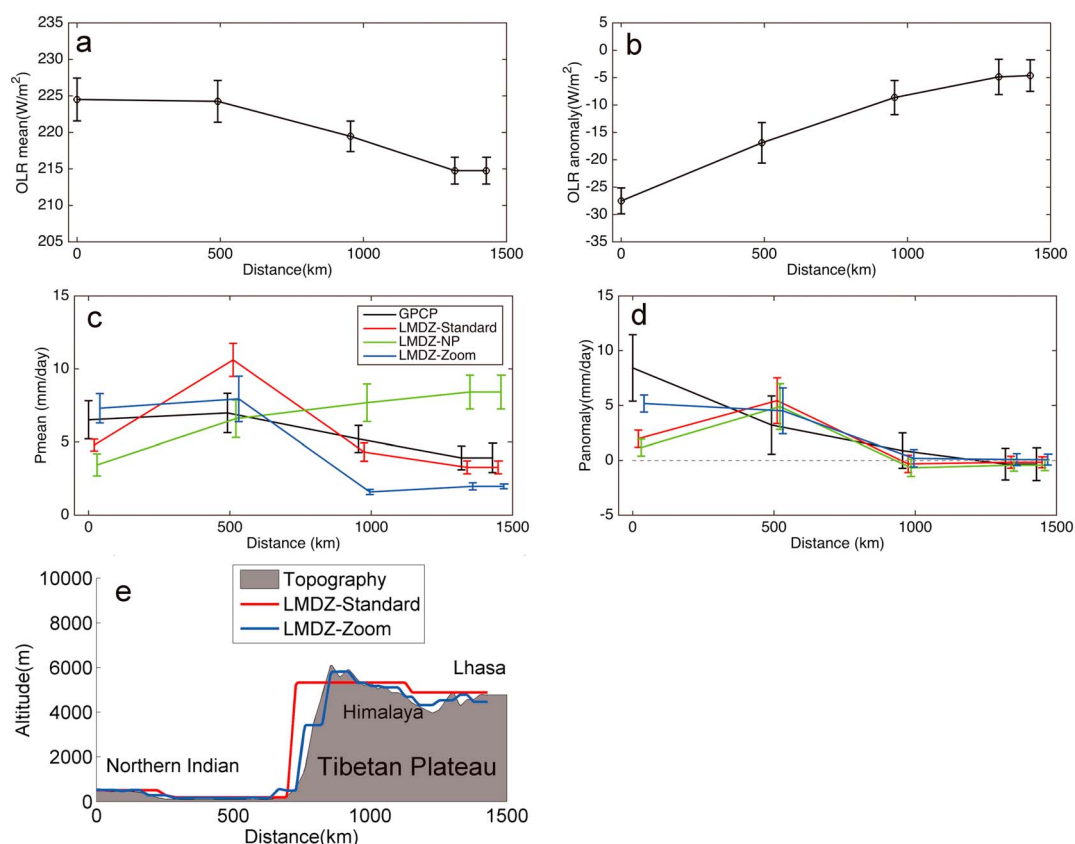


**Figure 11.** (a) Mean OLR along the back trajectory from Lhasa to Northern India and (b) OLR anomaly during LOW-OLR-NI conditions, with respect to JJAS mean values. (c, d) Same as Figures 11a and 11b but for precipitation. (e) Topography along the back trajectory. The definition of LOW-OLR-NI conditions is the same as in Figure 9. The error bars represent plus or minus twice the standard error ( $\epsilon$ ) of the mean value. This standard error  $\epsilon$  is calculated as the standard deviation of the anomaly values divided by the square root of the number of anomaly values. Twice  $\epsilon$  represent approximately the 95% confidence interval.

investigated in more detail. To do this, we examine days of strong convection in NI. When the NI OLR is lower than the JJAS mean OLR minus 40% of its standard deviation ( $28 \text{ W/m}^2$ ), the day is defined as a strong convection day. Results are not qualitatively sensitive to the 40% threshold. Altogether, we identify 121 strong convection days in JJAS from 2005 to 2007. We calculate a composite of various variables for these specific strong convection days, and compare results with JJAS mean conditions.

As shown in Figure 9, strong convection days are associated with positive surface  $q$  and negative  $\delta D_v$  anomaly. TES data depict positive anomalies of  $\delta D_v$  at middle and upper atmospheric levels (Figure 9c), where a positive cloud anomaly is evidenced by CALIPSO data (Figure 9e). Increased cloud cover is associated with enhanced convective detrainment, which is associated with higher upper troposphere  $\delta D_v$  values [Moyer *et al.*, 1996; Risi *et al.*, 2012; Worden *et al.*, 2013; Jiang *et al.*, 2013]. However, the positive middle-upper levels cloud anomaly at Lhasa are inconsistent with negative  $\delta D_v$  anomaly (Figures 9d and 9f).

LMDZiso Standard and Zoom versions reasonably reproduce the mean vertical structure of  $q$  and  $\delta D_v$ , while LMDZiso NP overestimates humidity and deuterium levels above NI. Differences between LMDZiso standard and zoom simulations are expected to arise from changes in topography. All LMDZiso versions reasonably capture the positive  $q$  anomaly associated with convection. However, all model versions fail to reproduce the positive  $\delta D_v$  anomaly at middle-upper levels (Figure 9c, right). This discrepancy is due to misrepresentation of the cloud vertical profile in LMDZiso. This is evidenced by comparing LMDZiso simulation to the CALIPSO data (Figure 9e). LMDZiso NP captures the positive cloud anomaly at upper atmospheric levels and thus reasonably reproduces the positive  $\delta D_v$  anomaly at this level. However, it fails to reproduce the positive  $\delta D_v$  anomaly in the middle troposphere, which may be due to the misrepresentation of the cloud fraction at this level. In comparison, LMDZiso Standard fails to reproduce both cloud and  $\delta D_v$  anomalies at middle and high levels.



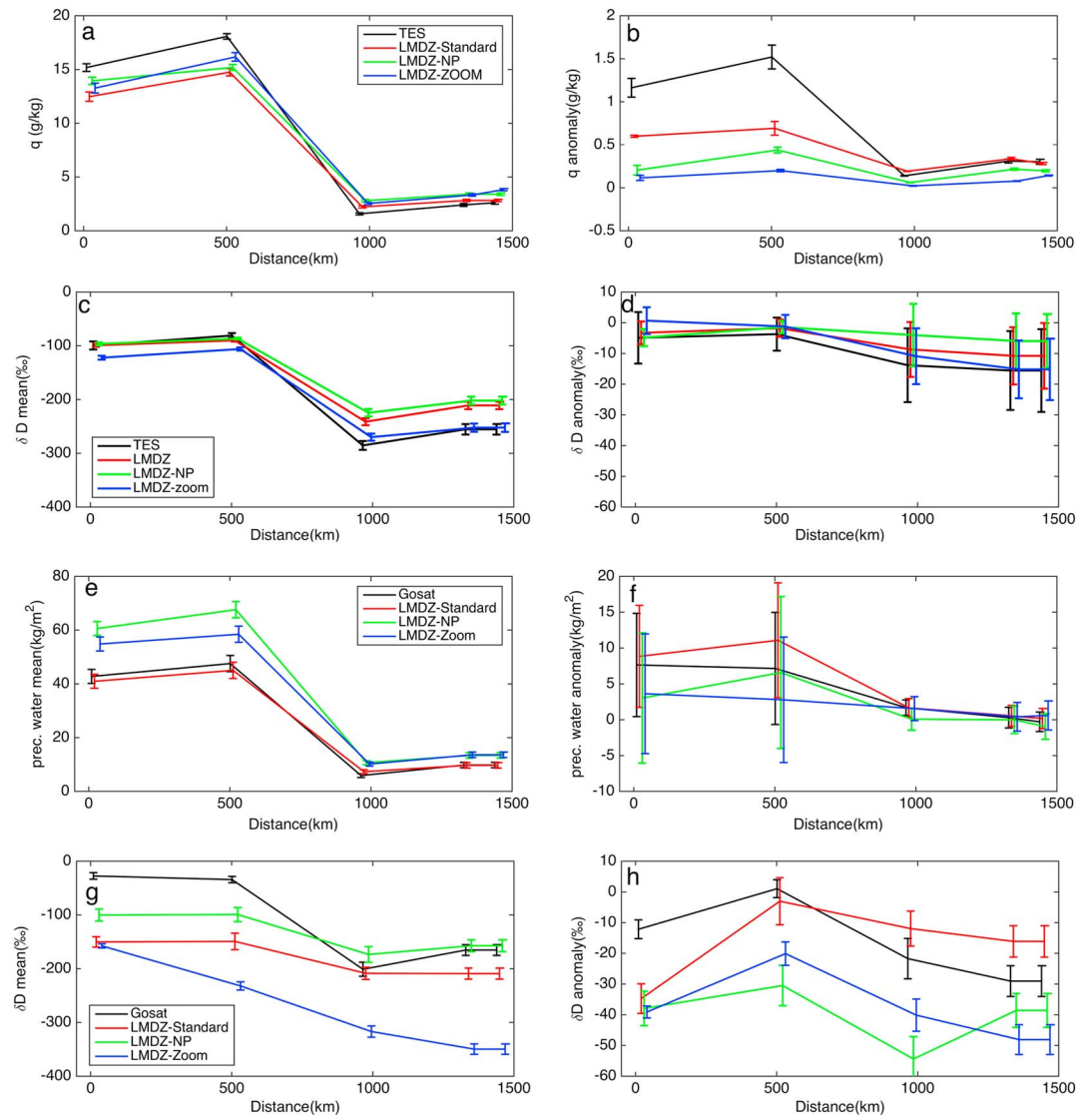


**Figure 12.** (a, c, e, and g) Mean observed and simulated values along the back trajectories. (b, d, f, and h) Anomalies during LOW-OLR-NI conditions respect to JJAS mean values. Specific humidity ( $q$ ) 100 hPa above the ground surface retrieved from TES (Figures 12a and 12b),  $\delta D_v$  100 hPa above the ground surface retrieved from TES (Figures 12c and 12d), precipitable water retrieved from GOSAT (Figures 12e and 12f), and column-integrated  $\delta D_v$  retrieved from GOSAT (Figures 12g and 12h). Outputs simulated by LMDZ have been collocated and convolved by the appropriate averaging kernels. The definition of LOW-OLR-NI conditions is the same as in Figure 9. The error bars report plus or minus twice standard error of the mean value.

We investigate the vertical profile of  $\delta D_v$  and cloud fraction at Lhasa 3 days after strong convection has occurred in NI. This lag was estimated from the correlation maps in Figure 7 and from the back trajectory analysis which is described in the next section.

#### 4.2. Evolution of Water Vapor $\delta D_v$ Along Air Mass Trajectory

As discussed above, LMDZiso fails to reproduce the vertical  $\delta D_v$  anomaly in NI. However, it does successfully capture the  $\delta D_v$  anomaly profile at Lhasa (Figure 9d). There is a positive relationship between  $\delta D_v$  in TES at Lhasa and OLR (Figure 6b), yet a negative relationship between middle-upper levels  $\delta D_v$  at NI and OLR (Figure 9c, right). We conclude that  $\delta D_v$  anomalies at Lhasa are neither controlled by local convection and clouds nor by NI cloud effects on the vertical  $\delta D_v$  profile in NI.

Back trajectories, launched from 1000 m AGL at Lhasa, were calculated for 5 days prior to launching in order to investigate the processes affecting the  $\delta D_v$  profile along the transport path. These back trajectories

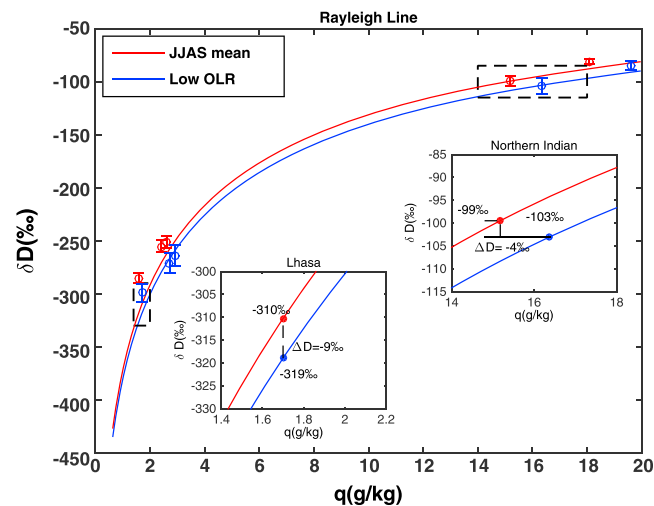


**Figure 13.** Rayleigh distillation theoretical line (solid line) and observed in TES (open circle) in a  $q$ - $\delta D_v$  diagram. The red line starts with JJAS mean conditions in Northern India (NI). The error bars report plus or minus twice standard error of the mean value. The blue line starts with LOW-OLR-NI conditions. The two subgraphs are centered on typical specific humidity values over Lhasa and NI. The definition of LOW-OLR-NI conditions is the same as in Figure 9.

mean wind transport between NI and Lhasa. It takes about 4 days for the air traveling from NI to Lhasa. This is consistent with the maximum positive correlation between Lhasa  $\delta D_v$  and NI OLR, obtained when OLR leads  $\delta D_v$  by 3 to 4 days. According to this average trajectory, the water vapor at Lhasa mainly travels from low levels above NI (Figure 10b), consistent with previous studies [Feng and Zhou, 2012]. Surface air masses may well ascend the Himalaya due to mechanical and thermal forcing over the TP [Ye, 1981; Wu and Zhang, 1998; Wu *et al.*, 2007].

To understand the evolution of  $\delta D_v$ , we need to understand the convection and condensation histories along the trajectory. Figure 11 shows the mean and anomaly (i.e., when OLR is low in NI) of both OLR and precipitation in JJAS along this trajectory. On average, OLR decreases from NI to the TP. Deeper into the TP, as air masses have already lost part of their moisture through rainout, precipitation amount decreases despite persistence of convective activity (Figures 11a and 11c). The OLR anomaly weakens along the trajectory from NI to Lhasa but remains negative. The small OLR anomaly near Lhasa is not significant. The precipitation anomaly identified from GPCP data decreases along the back trajectory, and it even becomes negative near Lhasa.

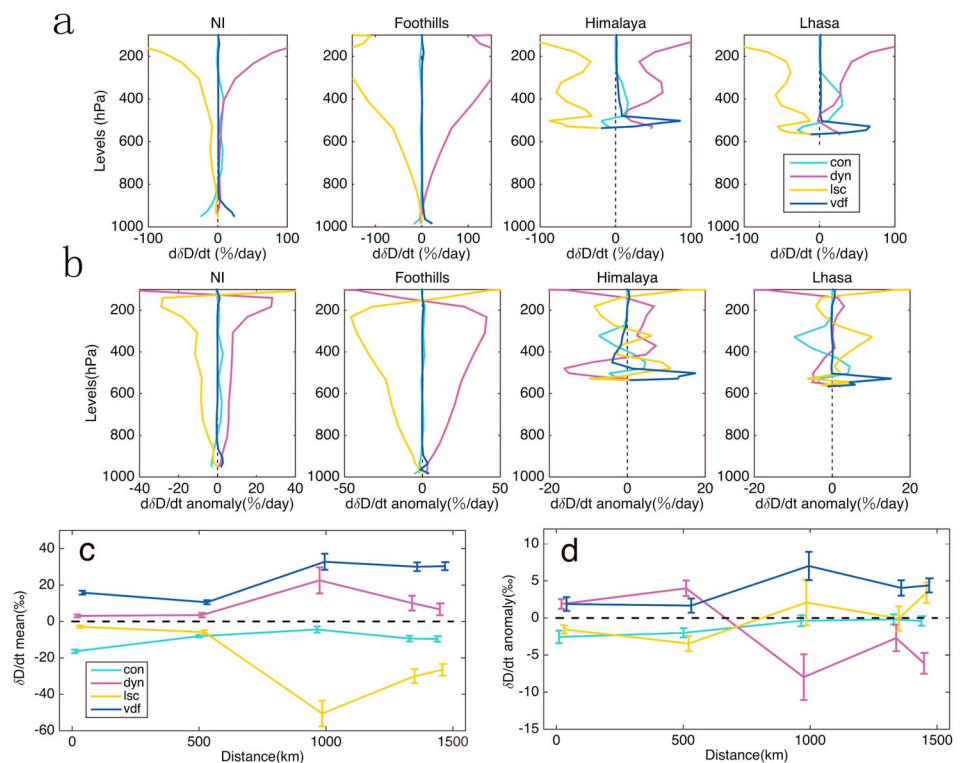
The LMDZiso Zoom and LMDZiso Standard both reasonably capture the mean precipitation amount along the average trajectory (Figure 11), but LMDZiso NP underestimates north Indian precipitation and strongly overestimates TP precipitation amount. It may thus misrepresent some processes controlling  $\delta D_v$  in TP. LMDZiso Zoom captures the positive TP precipitation anomaly associated with strong NI convection. LMDZiso NP and LMDZiso Standard exhibit a maximum precipitation anomaly value near the Himalaya foothills rather than in NI, where the largest precipitation is observed.

Figure 12 presents  $q$ ,  $\delta D_v$ , and precipitable water along the trajectory, retrieved from satellite, and simulated by LMDZiso. Because the back trajectories follow the topography, we plot  $q$  and  $\delta D_v$  at 100 hPa above the ground surface (Figures 12a and 12c). Since about 60% of the column-integrated water vapor is in the first 200 hPa above ground level regardless the topography, precipitable water, and total column  $\delta D_v$  along trajectory (Figures 12e and 12g) can be compared to  $q$  and  $\delta D_v$  at 100 hPa above the ground surface. On average, the evolution of precipitable water and total column  $\delta D_v$  follows to first order the topography (Figure 12a, 12c, 12e, and 12g). The uplift to high-altitude results in decreased  $q$  and lower  $\delta D_v$ .

The large positive  $q$  anomaly retrieved from TES during strong convection over the Himalaya foothills (Figure 12d) indicates that convection efficiently moistens air masses in this region. As already discussed, strong convection activities decrease the low-level  $\delta D_v$  in NI though there are large measurement

can be grouped into two categories. First, trajectories from the northern and western parts of the TP are associated with low water vapor content [Feng and Zhou, 2012]. They correspond to only 12% of the total precipitation amount at Lhasa in JJAS. The second class represents trajectories from the south, following the Indian monsoon, which transports considerable vapor amounts [Tian *et al.*, 2001a; Feng and Zhou, 2012], responsible for 88% of the total precipitation amount at Lhasa in JJAS.

To investigate the link between  $\delta D_v$  at Lhasa and convection in Northern India, we now focus on trajectories from the south. By averaging all trajectories, we produce a trajectory for a region from 75°E to 84°E and from 20°N to 26°N. Figure 10 shows these trajectories and the JJAS mean field from 2005 to 2007, consistent with the



**Figure 14.** Contributions to the isotopologue budget at four locations (NI, Foothills, Himalaya, and Lhasa) along the back trajectory, as computed by LMDZiso Standard. We show both JJAS mean values and anomalies during LOW-OLR-NI conditions with respect to JJAS mean values. The definition of LOW-OLR-NI conditions is the same as in Figure 9. The temporal derivative of  $\delta D_v$  is decomposed into the effect of convection (cyan), large-scale advection (red), large-scale condensation (green), and surface evaporation and boundary layer mixing (dark blue). See text for more detail. (a) Vertical distribution of contributions to the isotopologue budget and (b) anomalies during LOW-OLR-NI conditions. (c) Contribution to the isotopologue budget at 100 hPa above ground surface and (d) anomalies during LOW-OLR-NI conditions.

uncertainties (Figure 12d). This initial anomaly is then amplified as air ascend over the Himalaya. GOSAT observations show consistent results.

All LMDZiso versions capture reasonably well the mean  $q$ , mean  $\delta D_v$  and precipitable water along the trajectory (Figure 12a, 12c, and 12e). During strong convection days above NI, all LMDZiso versions reasonably reproduce the low values of local surface  $\delta D_v$  (except for the zoom model version in Figure 12d) and the amplification of  $\delta D_v$  anomalies over the Himalaya foothills, despite the difference in absolute values. Note that the LMDZiso NP simulation of  $\delta D_v$  is not superior despite the fact that this model version performs better for the simulation of cloud cover (Figures 9e and 9f, section 4.2).

#### 4.3. Amplification of $\delta D_v$ Anomalies Over the Foothills by Rayleigh Processes

Here we aim to explain the mechanism amplifying the depletion of the vapor in HDO over the Himalaya foothills, following strong convection above NI. We hypothesize that this enhanced convection produces moister air masses, followed by enhanced condensation during the uplift on the Himalayan foothills. This more intense condensation is expected to decrease isotopologue composition. To test this hypothesis, we assume that the orographic condensation over the foothills can be modeled as a simple Rayleigh distillation.

Figure 13 shows such Rayleigh distillation lines for JJAS mean conditions (red) and for days with strong convection in NI (blue), corresponding to the two types of NI initial conditions. At the start of the distillation line, the strong convection composite is characterized by water vapor with higher  $q$  and lower  $\delta D_v$  (by  $-4\text{‰}$ ). At the end of the distillation line, at Lhasa,  $q$  is almost the same for the strong convection composite and for the JJAS mean conditions. This implies that more water vapor has been condensed along the transport path for the strong convection composite. This enhanced condensation leads to  $\delta D_v$  at Lhasa being  $9\text{‰}$  lower for the composite than for JJAS mean conditions (Figure 13). This calculation supports our hypothesis that the  $\delta D_v$

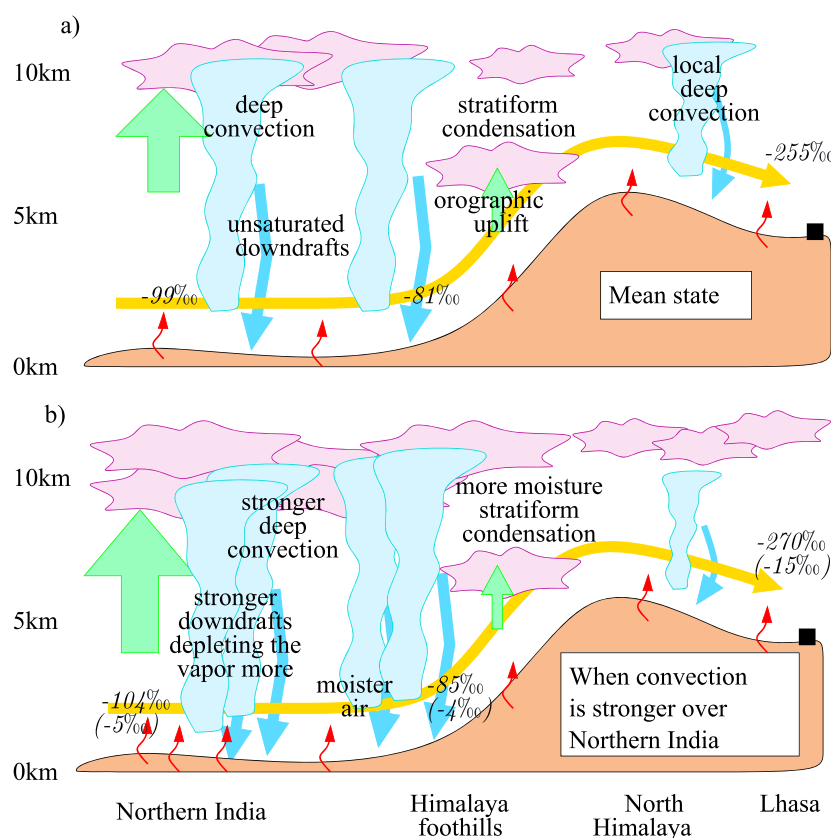


**Figure 15.** Summary of our understanding of how convection in NI affects  $\delta D_v$  over Lhasa along the back trajectory. The mean  $\delta D_v$  values (a) for the mean state and (b) for LOW-OLR-NI conditions are indicated in italic. In parentheses, the mean  $\delta D_v$  anomalies respect to mean state are also indicated. The definition of LOW-OLR-NI conditions is the same as in Figure 9. The green arrows represent large-scale vertical ascent. The yellow arrows represent the transport route from NI to Lhasa. The red arrows represent surface evaporation. The downward blue arrows represent unsaturated downdrafts.

anomaly amplification over the Himalaya foothills results from enhanced Rayleigh condensation processes. This is further supported by the large amount of precipitation over the Himalaya foothills.

Alternatively, the  $\delta D_v$  over the Himalaya foothills may also decrease when mixing occurs with air masses from BOB, with low  $\delta D_v$ . The BOB  $\delta D_v$  is about 6‰ lower for the days with strong convection in NI than JJAS mean conditions. Therefore, large-scale mixing [Galewsky and Hurley, 2010; Noone, 2012] could also play a role in the  $\delta D_v$  anomaly amplification.

#### 4.4. Detailed Analysis of the Influence of Convection, Large-Scale Condensation, and Water Vapor Transport in the LMDZ Model

We have previously shown that LMDZiso is able, despite some caveats, to capture many aspects of the observations. We now use LMDZiso simulations to understand the mechanisms explaining low  $\delta D_v$  at Lhasa. Only the results from the standard version are shown in Figure 14; similar results were found for other versions. For this purpose, we analyze the  $\delta D_v$  change in water vapor isotopologue composition (i.e.,  $\delta D_v$  change with time) along the pathway.

In LMDZiso, water vapor is decomposed into four contributions: (1) advection by the large-scale dynamics (dyn); (2) large-scale condensation (lsc) which include the effect of in situ condensation in stratiform and orographic clouds, and of the partial reevaporation of the precipitation; (3) convection (con) which includes the effects of unsaturated downdrafts, compensating subsidence, convective precipitation reevaporation and convective detrainment; and (4) surface evaporation and boundary layer mixing (vdf).

Figure 14 shows the vertical distribution of the four contributions to the  $\delta D_v$  from NI to Lhasa along the back trajectory. The moisture budget has a very similar behavior to that of the  $\delta D_v$  budget: moistening processes correspond to high  $\delta D_v$  and dehydrating processes correspond to low  $\delta D_v$ . For average JJAS conditions,

large-scale condensation (green) is always drying the vapor and lowering  $\delta D_v$ , while advection (red) has opposite effects. Near Lhasa, convection (cyan) dries low-level air and lessens low-level  $\delta D_v$  values but moistens middle to upper level air and increases middle to upper level  $\delta D_v$  values by detrainment. Finally, surface evaporation moistens low-level air and increases low-level  $\delta D_v$  values.

According to LMDZ, the combination of enhanced large-scale condensation in the middle and upper troposphere and enhanced convection near the surface (i.e., unsaturated downdrafts, left panels of Figure 14b) explains the coupling between strong convection and reduced  $\delta D_v$  in NI. This feature is simulated both in NI and over the Himalaya foothills. LMDZ simulation confirms our understanding of how stronger convection in NI leads to reduced  $\delta D_v$  in the low-level vapor in section 4.2. We also show change in the low-level vapor  $d\delta D_v/dt$  (100 hPa above the ground surface) along the back trajectory (Figures 14c and 14d). For the average JJAS conditions (Figure 14c), the unsaturated downdrafts and the large-scale condensation both contribute to the decrease in  $\delta D_v$  along the route to Lhasa. By contrast, both surface evaporation and advection increase  $\delta D_v$  along the pathway. Figure 15 summarizes our understanding of the processes controlling the intraseasonal variability of  $\delta D_v$  at Lhasa.  $\delta D_v$  values are more negative due to stronger unsaturated downdrafts over NI on days of strong convection. These values are further decreased by more large-scale condensation over the Himalaya foothills before the air masses are transported to Lhasa.

### Acknowledgments

This work is supported by CAS Strategic Priority Research Program(B)-Interactions among Multiple Geo-spheres on Tibetan Plateau and their Resource-Environment Effects (grant XDB03030100), by the National Natural Science Foundation of China (grants 41471053 and 41190080), and by the China-France Caiyuanpei Program. This work was finished in Laboratoire de Météorologie Dynamique, Institut Pierre Simon Laplace, CNRS, Paris, France. LMDZ simulations were performed on the supercomputer of the IDRIS computing center. Part of this research was carried out at the Jet Propulsion Laboratory, California Institute of Technology, under a contract with the National Aeronautics and Space Administration. C.-T. Lai was supported by the U.S. National Science Foundation, Division of Atmospheric and Geo-space Sciences under Grant AGS-0956425. We thank Laurent Li and Pang Hongxi for their constructive comments. We also thank the staffs from Tibet observation stations for collecting the samples and staffs for measuring the samples, and all those who contributed to the field work. Part of in situ  $\delta^{18}O_p$  data are from Third Pole Environment Database (<http://en.tpdatabase.cn/>). The back trajectories and the OLR (Outgoing Longwave Radiation) are computed using National Centers for Environmental Prediction (NCEP) reanalysis data. LMDZiso data can be acquired by contacting Camille Risi ([Camille.Risi@lmd.jussieu.fr](mailto:Camille.Risi@lmd.jussieu.fr)). TES and GOSAT satellite data can also be acquired by contacting John Worden ([john.r.worden@jpl.nasa.gov](mailto:john.r.worden@jpl.nasa.gov)). CALIPSO data can also be acquired by contacting Gregory Cesana ([gregory.cesana@lmd.polytechnique.fr](mailto:gregory.cesana@lmd.polytechnique.fr)). In situ  $\delta^{18}O_p$  data can also be acquired by contacting Gao Jing ([gaojing@itpcas.ac.cn](mailto:gaojing@itpcas.ac.cn)).

### 5. Conclusion

This study aims at investigating the processes controlling the day-to-day summer variability of isotopologue composition observed in the southern TP. At Lhasa, observed  $\delta^{18}O_p$  and  $\delta D_v$  are lowest in July and August when moisture arrives at the site from Northern India. LMDZiso captures many features of the observations and can thus be used as a powerful tool to understand processes controlling the intraseasonal variability of TP vapor and precipitation isotopologue composition.

Paleorecords of  $\delta^{18}O_p$  are archived directly or indirectly in tree rings, speleothems, lake sediments, and glacier ice. Our study has disentangled the processes at play for intraseasonal variations. However, in order to understand the paleoclimatic information preserved in natural archives from the southern TP, it is necessary to assess whether the underlying mechanisms responsible for the intraseasonal scale also explain the variability of the isotopologue signal at longer time scales, such as interannual, decadal, and also orbitally driven variations. Expanding this study to other regions of Tibet is also important, as ice core records from different regions of the southern TP reflect different control processes [Pang et al., 2014]. Intercomparing isotopic GCMs would allow us to investigate shortcomings in the model physics and to improve model's capability for simulating the Southern TP isotopologue variability.

### References

- Aggarwal, P. K., K. Fröhlich, K. M. Kulkarni, and L. L. Gourcy (2004), Stable isotope evidence for moisture sources in the Asian summer monsoon under present and past climate regimes, *Geophys. Res. Lett.*, *31*, L08203, doi:10.1029/2004GL019911.
- Araguas-Araguas, L., K. Fröhlich, and K. Rozanski (1998), Stable isotope composition of precipitation over southeast Asia, *J. Geophys. Res.*, *103*(D22), 28,721–28,742, doi:10.1029/98JD02582.
- Bao, Q., L. Pengfei, Z. Tianjun, and L. Yimin (2013), The flexible global ocean-atmosphere-land system model, spectral version 2: FGOALS-s2, *Adv. Atmos. Sci.*, *30*(3), 561–576, doi:10.1007/s00376-012-2113-9.
- Bodas-Salcedo, A., et al. (2011), COSP: Satellite simulation software for model assessment, *Bull. Am. Meteorol. Soc.*, *92*(8), 1023–1043, doi:10.1175/2011bams2856.1.
- Brown, D., J. Worden, and D. Noone (2008), Comparison of atmospheric hydrology over convective continental regions using water vapor isotope measurements from space, *J. Geophys. Res.*, *113*, D15124, doi:10.1029/2007JD009676.
- Chepfer, H., S. Bony, D. Winker, M. Chiriaco, J.-L. Dufresne, and G. Sèze (2008), Use of CALIPSO lidar observations to evaluate the cloudiness simulated by a climate model, *Geophys. Res. Lett.*, *35*, L15704, doi:10.1029/2008GL034207.
- Chepfer, H., S. Bony, D. Winker, G. Cesana, J. L. Dufresne, P. Minnis, C. J. Stubenrauch, and S. Zeng (2010), The GCM-Oriented CALIPSO Cloud Product (CALIPSO-GOCCP), *J. Geophys. Res.*, *115*, D00H16, doi:10.1029/2009JD012251.
- Coindreau, O., F. Hourdin, M. Haefelin, A. Mathieu, and C. Rio (2007), Assessment of physical parameterizations using a global climate model with stretchable grid and nudging, *Mon. Weather Rev.*, *135*(4), 1474–1489, doi:10.1175/mwr3338.1.
- Dansgaard, W., S. J. Johnsen, J. Møller, and C. C. Langway Jr. (1969), One thousand centuries of climatic record from Camp Century on the Greenland ice sheet, *Science*, *166*(3903), 377–380, doi:10.1126/science.166.3903.377.
- Draxler, R. R. (1998), An overview of the HYSPLIT4 modelling system for trajectories, dispersion, and deposition, *Bur. Meteorol. Res. Centre*, *47*, 295–308.
- Fabien, M., S. Dieter, M. Thomas, C. Emily, C. Julia, and F. Roman (2014), Precipitation seasonality and variability over the Tibetan Plateau as resolved by the high Asia reanalysis, *J. Clim.*, *27*, 1901–1927, doi:10.1175/JCLI-D-13-00282.1.
- Feng, L., and T. Zhou (2012), Water vapor transport for summer precipitation over the Tibetan Plateau: Multidata set analysis, *J. Geophys. Res.*, *117*, D20114, doi:10.1029/2011JD017012.
- Frankenberg, C., et al. (2009), Dynamic processes governing lower-tropospheric  $HDO/H_2O$  ratios as observed from space and ground, *Science*, *325*(5946), 1374–1377, doi:10.1126/science.1173791.



- Frankenberg, C., D. Wunch, G. Toon, C. Risi, R. Scheepmaker, J. E. Lee, P. Wennberg, and J. Worden (2013a), Water vapor isotopologues retrievals from high resolution GOSAT short-wave infrared spectra, *Atmos. Meas. Tech. Discuss.*, *5*(5), 6357–6386, doi:10.5194/amtd-5-6357-2012.
- Frankenberg, C., D. Wunch, G. Toon, C. Risi, R. Scheepmaker, J.-E. Lee, P. Wennberg, and J. Worden (2013b), Water vapor isotopologue retrievals from high-resolution GOSAT shortwave infrared spectra, *Atmos. Meas. Tech.*, *6*(2), 263–274, doi:10.5194/amt-6-263-2013.
- Fu, R., A. D. Del Genio, and W. B. Rossow (1990), Behavior of deep convective clouds in the tropical Pacific deduced from ISCCP radiances, *J. Clim.*, *3*(9–10), 1129–1152, doi:10.1175/1520-0442(1990)003<1129:BODCCI>2.0.CO;2.
- Galewsky, J., and J. V. Hurley (2010), An advection-condensation model for subtropical water vapor isotopic ratios, *J. Geophys. Res.*, *115*, D16116, doi:10.1029/2009JD013651.
- Gao, J., V. Masson-Delmotte, T. Yao, L. Tian, C. Risi, and G. Hoffmann (2011), Precipitation water stable isotopes in the South Tibetan Plateau: Observations and modeling, *J. Clim.*, *24*(13), 3161–3178, doi:10.1175/2010JCLI3736.1.
- Gao, J., V. Masson-Delmotte, C. Risi, Y. He, and T. Yao (2013), What controls precipitation  $\delta^{18}\text{O}$  in the southern Tibetan Plateau at seasonal and intra-seasonal scales? A case study at Lhasa and Nyalam, *Tellus B*, *65*, 21043, doi:10.3402/tellusb.v65i0.21043.
- Gates, W. L. (1992), AMIP: The Atmospheric Model Intercomparison Project, *Bull. Am. Meteorol. Soc.*, *73*(12), 1962–1970.
- Goswami, B. N. (2005), Intraseasonal variability (ISV) of South Asian summer monsoon, in *Intraseasonal Variability of the Atmosphere-Ocean Climate System*, pp. 19–61, Springer, Berlin.
- Grandpeix, J.-Y., and J.-P. Lafore (2010), A density current parameterization coupled with Emanuel's Convection Scheme. Part I: The models, *J. Atmos. Sci.*, *67*(4), 881–897, doi:10.1175/2009JAS3044.1.
- Hollaway, C. E., and J. D. Neelin (2010), Temporal relations of column water vapor and tropical precipitation, *J. Atmos. Sci.*, *67*(4), 1091–1105, doi:10.1175/2009JAS3284.1.
- Hourdin, F., et al. (2006), The LMDZ4 general circulation model: Climate performance and sensitivity to parametrized physics with emphasis on tropical convection, *Clim. Dyn.*, *27*(7–8), 787–813, doi:10.1007/s00382-006-0158-0.
- Hourdin, F., et al. (2013), LMDZ5B: The atmospheric component of the IPSL climate model with revisited parameterizations for clouds and convection, *Clim. Dyn.*, *40*(9–10), 2193–2222, doi:10.1007/s00382-012-1343-y.
- Huffman, G. J., R. F. Adler, M. M. Morrissey, D. T. Bolvin, S. Curtis, R. Joyce, B. McGavock, and J. Susskind (2001), Global precipitation at one-degree daily resolution from multisatellite observations, *J. Hydrometeorol.*, *2*(1), 36–50, doi:10.1175/1525-7541(2001)002<0036:gpaodd>2.0.co;2.
- Jiang, Z., D. B. A. Jones, H. M. Worden, M. N. Deeter, D. K. Henze, J. Worden, K. W. Bowman, C. A. M. Brenninkmeijer, and T. J. Schuck (2013), Impact of model errors in convective transport on CO source estimates inferred from MOPITT CO retrievals, *J. Geophys. Res. Atmos.*, *118*, 2073–2083, doi:10.1002/jgrd.50216.
- Jouzel, J., C. Lorius, J. R. Petit, C. Genthon, N. I. Barkov, V. M. Kotlyakov, and V. M. Petrov (1987), Vostok ice core: A continuous isotope temperature record over the last climatic cycle (160,000 years), *Nature*, *329*(6138), 403–408, doi:10.1038/329403a0.
- Jouzel, J., G. Delaygue, A. Landais, V. Masson-Delmotte, C. Risi, and F. Vimeux (2013), Water isotopes as tools to document oceanic sources of precipitation, *Water Resour. Res.*, *49*, 7469–7486, doi:10.1002/2013wr013508.
- Klinker, E., F. Rabier, G. Kelly, and J.-F. Mahfouf (2000), The ECMWF operational implementation of four-dimensional variational assimilation. III: Experimental results and diagnostics with operational configuration, *Q. J. R. Meteorol. Soc.*, *126*, 1191–1215, doi:10.1002/qj.49712656417.
- Krinner, G., C. Genthon, Z.-X. Li, and P. Le Van (1997), Studies of the Antarctic climate with a stretched-grid general circulation model, *J. Geophys. Res.*, *102*(D12), 13,731–13,745, doi:10.1029/96JD03356.
- Lacour, J. L., C. Risi, L. Clarisse, S. Bony, D. Hurtmans, C. Clerbaux, and P. F. Coheur (2012), Mid-tropospheric AD observations from IASI/MetOp at high spatial and temporal resolution, *Atmos. Chem. Phys.*, *12*(22), 10,817–10,832, doi:10.5194/acp-12-10817-2012.
- Lawrence, J. R., S. D. Gedzelman, D. Dexheimer, H.-K. Cho, G. D. Carrie, R. Gasparini, C. R. Anderson, K. P. Bowman, and M. I. Biggerstaff (2004), Stable isotopic composition of water vapor in the tropics, *J. Geophys. Res.*, *109*, D06115, doi:10.1029/2003JD004046.
- Lee, J., J. Worden, D. Noone, K. Bowman, A. Eldering, A. LeGrande, J. L. F. Li, G. Schmidt, and H. Sodemann (2011), Relating tropical ocean clouds to moist processes using water vapor isotope measurements, *Atmos. Chem. Phys.*, *11*(2), 741–752.
- Lee, J.-E., and I. Fung (2008), Amount effect of water isotopes and quantitative analysis of post-condensation processes, *Hydrol. Processes*, *22*(1), 1–8, doi:10.1002/hyp.6637.
- Lee, J.-E., C. Risi, I. Fung, J. Worden, R. A. Scheepmaker, B. Lintner, and C. Frankenberg (2012), Asian monsoon hydrometeorology from TES and SCIAMACHY water vapor isotope measurements and LMDZ simulations: Implications for speleothem climate record interpretation, *J. Geophys. Res.*, *117*, D15112, doi:10.1029/2011JD017133.
- LeGrande, A. N., G. A. Schmidt, and G. Hoffmann (2009), Sources of Holocene variability of oxygen isotopes in paleoclimate archives, *Clim. Past*, *5*(3), 441–455, doi:10.5194/cp-5-441-2009.
- Liebmann, B., and C. A. Smith (1996), Description of a complete (Interpolated) outgoing longwave radiation dataset, *Bull. Am. Meteorol. Soc.*, *77*(6), 1275–1277.
- Mölg, T., F. Maussion, and D. Scherer (2014), Mid-latitude westerlies as a driver of glacier variability in monsoonal High Asia, *Nat. Clim. Change*, *4*, 68–73, doi:10.1038/nclimate2055.
- Moore, M., Z. Kuang, and P. N. Blossey (2014), A moisture budget perspective of the amount effect, *Geophys. Res. Lett.*, *41*, 1329–1335, doi:10.1002/2013GL058302.
- Moyer, E. J., F. W. Irion, Y. L. Yung, and M. R. Gunson (1996), ATMOS stratospheric deuterated water and implications for troposphere-stratosphere transport, *Geophys. Res. Lett.*, *23*(17), 2385–2388, doi:10.1029/96GL01489.
- Noone, D. (2012), Pairing measurements of the water vapor isotope ratio with humidity to deduce atmospheric moistening and dehydration in the tropical midtroposphere, *J. Clim.*, *25*(13), 4476–4494, doi:10.1175/JCLI-D-11-00582.1.
- Pang, H., S. Hou, S. Kaspari, and P. A. Mayewski (2014), Influence of regional precipitation patterns on stable isotopes in ice cores from the central Himalayas, *The Cryosphere*, *8*(1), 289–301, doi:10.5194/tc-8-289-2014.
- Rajamani, S., and D. Sikdar (1989), Some dynamical characteristics and thermal structure of monsoon depressions over the Bay of Bengal, *Tellus A*, *41A*, 255–269, doi:10.1111/j.1600-0870.1989.tb00380.x.
- Rio, C., F. Hourdin, J. Y. Grandpeix, and J. P. Lafore (2009), Shifting the diurnal cycle of parameterized deep convection over land, *Geophys. Res. Lett.*, *36*, L07809, doi:10.1029/2008GL036779.
- Rio, C., et al. (2013), Control of deep convection by sub-cloud lifting processes: The ALP closure in the LMDZ5B general circulation model, *Clim. Dyn.*, *40*(9–10), 2271–2292, doi:10.1007/s00382-012-1506-x.
- Risi, C., S. Bony, and F. Vimeux (2008a), Influence of convective processes on the isotopic composition ( $\delta^{18}\text{O}$  and  $\delta\text{D}$ ) of precipitation and water vapor in the tropics: 2. Physical interpretation of the amount effect, *J. Geophys. Res.*, *113*, D19306, doi:10.1029/2008JD009943.

- Risi, C., S. Bony, F. Vimeux, L. Descroix, B. Ibrahim, E. Lebreton, I. Mamadou, and B. Sultan (2008b), What controls the isotopic composition of the African monsoon precipitation? Insights from event-based precipitation collected during the 2006 AMMA field campaign, *Geophys. Res. Lett.*, **35**, L24808, doi:10.1029/2008GL035920.
- Risi, C., S. Bony, F. Vimeux, C. Frankenberg, D. Noone, and J. Worden (2010a), Understanding the Sahelian water budget through the isotopic composition of water vapor and precipitation, *J. Geophys. Res.*, **115**, D24110, doi:10.1029/2010JD014690.
- Risi, C., S. Bony, F. Vimeux, and J. Jouzel (2010b), Water-stable isotopes in the LMDZ4 general circulation model: Model evaluation for present-day and past climates and applications to climatic interpretations of tropical isotopic records, *J. Geophys. Res.*, **115**, D12118, doi:10.1029/2009JD013255.
- Risi, C., et al. (2012), Process-evaluation of tropospheric humidity simulated by general circulation models using water vapor isotopic observations: 2. Using isotopic diagnostics to understand the mid and upper tropospheric moist bias in the tropics and subtropics, *J. Geophys. Res.*, **117**, D05304, doi:10.1029/2011JD016623.
- Risi, C., D. Noone, C. Frankenberg, and J. Worden (2013), Role of continental recycling in intraseasonal variations of continental moisture as deduced from model simulations and water vapor isotopic measurements, *Water Resour. Res.*, **49**, 4136–4156, doi:10.1002/wrcr.20312.
- Samuels-Crow, K. E., J. Galewsky, D. R. Hardy, Z. D. Sharp, J. Worden, and C. Braun (2014), Upwind convective influences on the isotopic composition of atmospheric water vapor over the tropical Andes, *J. Geophys. Res. Atmos.*, **119**, 7051–7063, doi:10.1002/2014JD021487.
- Schmidt, G. A., A. N. LeGrande, and G. Hoffmann (2007), Water isotope expressions of intrinsic and forced variability in a coupled ocean-atmosphere model, *J. Geophys. Res.*, **112**, D10103, doi:10.1029/2006JD007781.
- Thompson, L. G. (2000), A high-resolution millennial record of the South Asian monsoon from Himalayan Ice Cores, *Science*, **289**(5486), 1916–1919, doi:10.1126/science.289.5486.1916.
- Tian, L. (2003), Oxygen-18 concentrations in recent precipitation and ice cores on the Tibetan Plateau, *J. Geophys. Res.*, **108**(D9), 4293, doi:10.1029/2002JD002173.
- Tian, L., V. Masson-Delmotte, M. Stievenard, T. Yao, and J. Jouzel (2001a), Tibetan Plateau summer monsoon northward extent revealed by measurements of water stable isotopes, *J. Geophys. Res.*, **106**(D22), 28,081–28,088, doi:10.1029/2001JD00186.
- Tian, L., T. Yao, W. Sun, M. Stievenard, and J. Jouzel (2001b), Relationship between  $\delta D$  and  $\delta^{18}O$  in precipitation on north and south of the Tibetan Plateau and moisture recycling, *Sci. China, Ser. D Earth Sci.*, **44**(9), 789–796, doi:10.1007/BF02907091.
- Tremoy, G., F. Vimeux, S. Mayaki, I. Souley, O. Cattani, C. Risi, G. Favreau, and M. Oi (2012), A 1-year long  $\delta^{18}O$  record of water vapor in Niamey (Niger) reveals insightful atmospheric processes at different timescales, *Geophys. Res. Lett.*, **39**, L08805, doi:10.1029/2012GL051298.
- Vimeux, F., R. Gallaire, S. Bony, G. Hoffmann, and J. Chiang (2005), What are the climate controls on  $\delta D$  in precipitation in the Zongo Valley (Bolivia)? Implications for the Illimani ice core interpretation, *Earth Planet. Sci. Lett.*, **240**(2), 205–220, doi:10.1016/j.epsl.2005.09.031.
- Vimeux, F., G. Tremoy, C. Risi, and R. Gallaire (2011), A strong control of the South American SeeSaw on the intra-seasonal variability of the isotopic composition of precipitation in the Bolivian Andes, *Earth Planet. Sci. Lett.*, **307**(1–2), 47–58, doi:10.1016/j.epsl.2011.04.031.
- Vuille, M., M. Werner, R. S. Bradley, and F. Keimig (2005), Stable isotopes in precipitation in the Asian monsoon region, *J. Geophys. Res.*, **110**, D23108, doi:10.1029/2005JD006022.
- Wang, A., and X. Zeng (2012), Evaluation of multireanalysis products with in situ observations over the Tibetan Plateau, *J. Geophys. Res.*, **117**, D05102, doi:10.1029/2011JD016553.
- Wang, B., and Z. Fan (1999), Choice of South Asian summer monsoon indices, *Bull. Am. Meteorol. Soc.*, **80** (4), 629–638, doi:10.1016/j.epsl.2011.04.031.
- Winker, D. M., W. H. Hunt, and M. J. McGill (2007), Initial performance assessment of CALIOP, *Geophys. Res. Lett.*, **34**, L19803, doi:10.1029/2007GL030135.
- Worden, J., S. S. Kulawik, M. W. Shephard, S. A. Clough, H. Worden, K. Bowman, and A. Goldman (2004), Predicted errors of tropospheric emission spectrometer nadir retrievals from spectral window selection, *J. Geophys. Res.*, **109**, D09308, doi:10.1029/2004JD004522.
- Worden, J., et al. (2006), Tropospheric Emission Spectrometer observations of the tropospheric HDO/H<sub>2</sub>O ratio: Estimation approach and characterization, *J. Geophys. Res.*, **111**, D16309, doi:10.1029/2005JD006606.
- Worden, J., D. Noone, and K. Bowman (2007), Importance of rain evaporation and continental convection in the tropical water cycle, *Nature*, **445**(7127), 528–532, doi:10.1038/nature05508.
- Worden, J., S. Kulawik, C. Frankenberg, V. Payne, K. Bowman, K. Cady-Peirara, K. Wecht, J. E. Lee, and D. Noone (2012), Profiles of CH<sub>4</sub>, HDO, H<sub>2</sub>O, and N<sub>2</sub>O with improved lower tropospheric vertical resolution from Aura TES radiances, *Atmos. Meas. Tech.*, **5**(2), 397–411, doi:10.5194/amt-5-397-2012.
- Worden, J., et al. (2013), El Niño, the 2006 Indonesian peat fires, and the distribution of atmospheric methane, *Geophys. Res. Lett.*, **40**, 4938–4943, doi:10.1002/grl.50937.
- Wu, G., and Y. Zhang (1998), Tibetan Plateau forcing and the timing of the monsoon onset over South Asia and the South China Sea, *Mon. Weather Rev.*, **126**(4), 913–927, doi:10.1175/1520-0493(1998)126<0913:tpf>2.0.co;2.
- Wu, G., Y. Liu, Q. Zhang, A. Duan, T. Wang, R. Wan, X. Liu, W. Li, Z. Wang, and X. Liang (2007), The influence of mechanical and thermal forcing by the Tibetan Plateau on Asian climate, *J. Hydrometeorol.*, **8**(4), 770–789, doi:10.1175/jhm609.1.
- Yao, T., L. G. Thompson, E. Mosley-Thompson, Y. Zhihong, Z. Xingping, and P.-N. Lin (1996), Climatological significance of  $\delta^{18}O$  in north Tibetan ice cores, *J. Geophys. Res.*, **101**(D23), 29,531–29,537, doi:10.1029/96JD02683.
- Yao, T., et al. (2012), Different glacier status with atmospheric circulations in Tibetan Plateau and surroundings, *Nat. Clim. Change*, **2**, 663–667, doi:10.1038/nclimate1580.
- Yao, T., et al. (2013), A review of climatic controls on  $\delta^{18}O$  in precipitation over the Tibetan Plateau: Observations and simulations, *Rev. Geophys.*, **51**, 525–548, doi:10.1002/rog.20023.
- Ye, D. (1981), Some characteristics of the summer circulation over the Qinghai-Xizang (Tibet) Plateau and its neighborhood, *Bull. Am. Meteorol. Soc.*, **62**(1), 14–19, doi:10.1175/1520-0477(1981)062<0014:scotsc>2.0.co;2.
- You, Q., K. Fraedrich, G. Ren, B. Ye, X. Meng, and S. Kang (2012), Inconsistencies of precipitation in the eastern and central Tibetan Plateau between surface adjusted data and reanalysis, *Theor. Appl. Climatol.*, **109**(3–4), 485–496, doi:10.1007/s00704-012-0594-1.
- Yu, W., T. Yao, L. Tian, Y. Ma, K. Ichyanagi, Y. Wang, and W. Sun (2008), Relationships between  $\delta^{18}O$  in precipitation and air temperature and moisture origin on a south-north transect of the Tibetan Plateau, *Atmos. Res.*, **87**(2), 158–169, doi:10.1016/j.atmosres.2007.08.004.
- Yu, W., Y. Tandong, K. Shichang, P. Jianchen, and Y. Wei (2013), Different region climate regimes and topography affect the changes in area and mass balance of glaciers on the north and south slopes of the same glacierized massif (the West Nyainqentangliha Range, Tibetan Plateau), *J. Hydrol.*, **495**, 64–73, doi:10.1016/j.jhydrol.2013.04.034.
- Zhang, C. (1993), Large-scale variability of atmospheric deep convection in relation to sea surface temperature in the tropics, *J. Clim.*, **6**, 1898–1913, doi:10.1175/1520-0442(1993)006<1898:LVSOD>2.0.CO;2.